



Flow of mono-dispersed particles through horizontal bend

D.R. Kaushal ^{a,*}, A. Kumar ^b, Yuji Tomita ^c, Shigeru Kuchii ^d, Hiroshi Tsukamoto ^d

^a Department of Civil Engineering, IIT Delhi, Hauz Khas, New Delhi 110 016, India

^b Department of Mechanical Engineering, YMCA UST, Faridabad, Haryana, India

^c Kyushu Institute of Technology, 1-1 Sensui cho, Tobata, Kitakyushu 804-8550, Japan

^d Kitakyushu National College of Technology, 5-20-1 Shii, Kokura-minami, Kitakyushu 802-0985, Japan

ARTICLE INFO

Article history:

Received 11 June 2011

Received in revised form 30 December 2012

Accepted 31 December 2012

Available online 10 January 2013

Keywords:

CFD modeling

Eulerian model

Bend radius ratio

Pipe bend

Concentration distribution

Slurry pipeline

Pressure drop

ABSTRACT

Pipeline slurry flow of mono-dispersed particles through horizontal bend is numerically simulated by implementing Eulerian two-phase model in FLUENT software. A hexagonal shape and Cooper type non-uniform three-dimensional grid is chosen to discretize the entire computational domain, and a control volume finite difference method is used to solve the governing equations. The modeling results are compared with the experimental data collected in 53.0 mm diameter horizontal bend with radius of 148.4 mm for concentration profiles and pressure drops. Experiments are performed on narrow-sized silica sand with mean diameter of 450 μm and for flow velocity up to 3.56 m/s (namely, 1.78, 2.67 and 3.56 m/s) and four efflux concentrations up to 16.28% (namely, 0%, 3.94%, 8.82% and 16.28%) by volume for each velocity. Eulerian model gives fairly accurate predictions for both the pressure drop and concentration profiles at all efflux concentrations and flow velocities.

© 2013 Published by Elsevier Ltd.

1. Introduction

Pipe bends are an integral part of any pipeline network system as these provide flexibility in routing. The pressure loss in slurry flow through a bend is a strong function of the solids concentration, pipe diameter, flow velocity, bend radius, bend angle, size and specific gravity of particles. The secondary flow generated not only influences the pressure loss but also the distribution of solids leading to excessive wear.

Studies in bends for solid-liquid two-phase flow are few in number. Toda et al. (1972) experimentally determined the pressure drop over a length of 5.0 m including the pipe bend either in horizontal plane or vertical upward plane for the flow of glass beads of diameter 0.5–2.0 mm and polystyrene of diameter 1.0 mm, separately, using water as the carrier fluid. The four 90° pipe bends studied had R/r of 0, 2.4, 4.8 and 9.6, where r is the pipe radius and R is the bend radius. The pipe bends were made of poly-acrylate. For the bend in horizontal plane, they observed the sand particles move up along the inside wall at low velocity, while in straight pipe the flow is a sliding bed. They also found that even when a stationary bed was formed on the bottom of straight pipe, almost all particles were suspended in the pipe bend. At higher velocities, they observed that the particles were forced towards

the outer wall as a result of centrifugal forces generated in the bend. For bends in vertical plane, they observed that almost all the particles were travelling along the outside of the pipe bend. The solids were re-distributed downstream of the bend, the distance increasing with increase in velocity. They attributed this phenomenon to the increasing effect of centrifugal force as compared to the secondary flow.

Kalyanraman et al. (1973) have experimentally investigated the flow through 90° horizontal bend for sand-water slurry (sand particles having diameter of 2 mm) for different R/r at solid concentration varying between 0% and 18%. They have established that bend with $R/r = 5$ is optimum for the minimum pressure loss.

Turian et al. (1998) experimentally determined the friction losses for the flow of slurries of laterite and gypsum at efflux concentrations from 3.6% to 12.7% and from 10.7% to 30.6%, respectively, through 2.5 and 5.0 cm diameter pipe bends. For flow through 45° and 180° bends, and 90° bends having R/r in the range from 2 to 100, resistance coefficients were found to be inversely proportional to the Reynolds number for laminar flow, and to approach constant asymptotic values for turbulent flow.

Based on the above literature review, it is observed that studies related to the measurement of pressure drop and concentration profile around the bend for mono-dispersed particles are few, then what to say about multisized particles. In any practical situation, the solids that are being transported hydraulically through pipeline and bend are multisized and in fact their size may span three or

* Corresponding author. Tel.: +91 9818280867; fax: +91 11 2658 1117.

E-mail address: kaushal@civil.iitd.ac.in (D.R. Kaushal).

more orders of magnitude. The flow behavior of multisized is bound to be different from mono-dispersed due to redistribution of particles around the bend.

CFD based approach for investigating the variety of multiphase fluid flow problems in closed conduits and open channel is being increasingly used. One advantage with CFD-based approach is that three dimensional solid–liquid two phase flow problems under a wide range of flow conditions and sediment characteristics may be evaluated rapidly, which is almost impossible experimentally. Thinglas and Kaushal (2008a,b) have recently performed three-dimensional CFD modeling for optimization of invert trap configuration used in sewer solid management. Invert traps are sumps in the sewer invert and they have been used to collect the sediments within the sewers or drains. However, the use of such methodology for evaluating flow characteristics in slurry pipelines is limited. Ling et al. (2003) proposed a simplified three-dimensional algebraic slip mixture (ASM) model to obtain the numerical solution in sand–water slurry flow. Kumar et al. (2008) compared their preliminary experimental data of pressure drop with CFD modeling for slurry flow in pipe bend at concentrations of 3.94% and 8.82%.

In the present study, three-dimensional concentration distributions and pressure drops are calculated using Eulerian two-phase model in a 90 degree horizontal pipe bend having bend radius of 148.4 mm with pipe diameter of 53.0 mm at different efflux volumetric concentrations of mono-dispersed silica sand in the range from 0% to 16.28%. For each concentration, the flow velocity was varied from 1.78 to 3.56 m/s. The modeling results are compared with the experimental data.

2. Experimental setup

The pilot plant test loop of length 30 m with inside diameter being 53.0 mm as shown in Fig. 1 is used in the present study. Details of the loop are given elsewhere (Kumar, 2010). The distance between the two parallel horizontal pipes in Fig. 1 is 6.5 m. The pipe bend is laid horizontally. The slurry is prepared in the mixing

tank (2.73 m³), provided with a stirring arrangement to keep the slurry well mixed.

According to Ito (1960), the bend having a radius ratio of around 5.5 gives the minimum pressure drop in smooth bends for flow of water. Commercially available bends are not smooth and therefore it is decided in the present study to carry out the experiments with rough bends ($H_s/D = 0.0003$, where H_s is the average pipe wall roughness and D is the pipe diameter) having radius ratios around 5 for flow of water. Geometric details of all these pipe bends are tabulated in Table 1. The pipe bend having $R/r = 0$ is a sharp elbow consisting of two tubes with a 45° cut joined at an angle of 90°. Experimental and CFD modeling results obtained in the present study in seven different R/r ratios indicate that $R/r = 5.60$ gives the minimum pressure drop for flow of water in rough pipe bend. The bend geometry having a radius ratio R/r of 5.60 is therefore chosen in the present study for flow of silica sand particles.

The measured specific gravity of silica sand is 2.65 and the particles are having median particle size of 450 µm. The width of a particle size distribution is usually defined by the geometric standard deviation $\sigma_g = (d_{84.1}/d_{15.9})^{1/2}$, where $d_{84.1}$ and $d_{15.9}$ are particle diameters having 84.1% and 15.9% finer particles, respectively]. The geometric standard deviation σ_g for the particles used in the present study is found as 1.15.

Table 1
Geometric details of 90° horizontal bends used in flow of water.

Bend No.	Radius of curvature of Bend (R , mm)	Radius ratio (R/r)	Length of pipe bend
1	0	0	1.00D
2	79.1	2.98	2.34D
3	94.7	3.57	2.81D
4	111.8	4.22	3.31D
5	131.1	4.95	3.90D
6	148.4	5.60	4.40D
7	156.0	5.89	4.62D

$D = 53$ mm, $H_s/D = 0.0003$.

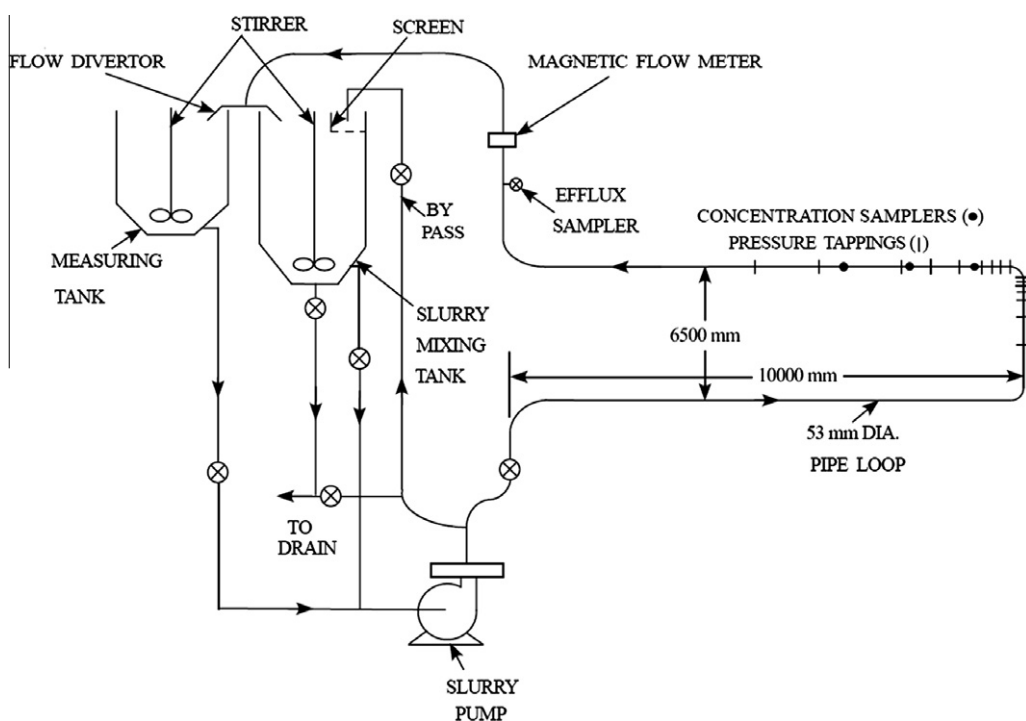


Fig. 1. Schematic diagram of pilot plant test loop.

In the straight pipeline, a small length of perspex pipe was provided (designated as observation chamber) to establish the critical deposition velocity of the slurry in the pipeline by observing the motion of the particles at the bottom of the pipeline. Critical deposition velocity is the flow velocity at which the particles start settling at pipe bottom. Measurement of critical deposition velocity showed no significant change with efflux concentration. It is observed that deposition velocity increases only by a very little amount as efflux concentration increases. Deposition velocity varied from 1.50 m/s to 1.55 m/s in the range of efflux concentration from 3.94% to 16.28% by volume. Similar observations for critical deposition velocity have been made by Schaan et al. (2000) in the flow of spherical glass beads, Ottawa sand and Lane mountain sand slurries through 105 mm diameter pipe. They found critical deposition velocity for spherical glass beads as constant over the range of solids concentrations from 5% to 45% by volume. For Ottawa sand and Lane mountain sand slurries, they reported only a little increase of around 0.2 m/s in critical deposition velocity in the range of solids concentrations from 5% to 30% by volume. Kaushal and Tomita (2002) experimentally observed a variation in critical deposition velocity from 1.10 m/s to 1.18 m/s in the range of efflux concentration from 4 % to 26 % by volume for multisized particulate zinc tailings slurry flowing through 105 mm diameter horizontal pipe.

The test bend of radius ratio 5.60 as shown in Fig. 2 is fitted in the test loop. The minimum straight length at the upstream of bend is more than 100D (6.5 m as shown in Fig. 1) which ensures fully developed flow at the test bend inlet. The downstream length helps to measure the pressure loss and effect of bend on the solid re-distribution in the downstream straight section. The straight length downstream of the bend is more than 140D (10 m as shown in Fig. 1).

To measure the pressure drop distribution along the bends, pressure taps were provided on the upstream and downstream sides of the bends at different points. Pressure drops are measured in the pipeline at 0, D, 2D, 4D, 8D, 16D, 32D, 64D, and 90D in the

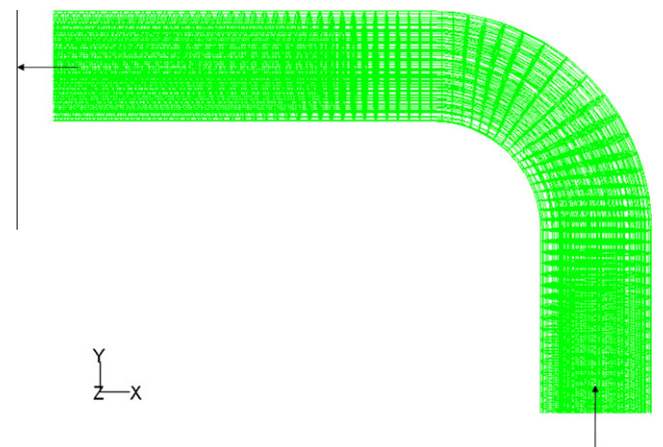


Fig. 3. Enlarged view of meshing in pipe bend.

downstream of the bend exit and 0, D, 2D, 4D, 8D, 16D and 32D in the upstream of the bend inlet as shown in Fig. 2.

In order to account for the disturbed flow conditions, two pressure taps are provided at diametrically opposite positions in the horizontal plane at each location. The pressure is not uniform across the bend cross-section and increases from the inner wall to the outer wall. Pressure is also decreasing along the bend continuously from inlet to exit of the bend. It is true that more pressure taps would have given average pressure at a location more precisely and thus more accurate pressure drop along the bend. However, in view of smaller pipe diameter of 53.0 mm, it was decided to use only two pressure taps at each location.

Two different pressure drops are measured at diametrically opposite positions in the horizontal plane at each location with respect to a reference location which is chosen as 32D upstream of the bend inlet. Multi-tube, inverted U-tube manometer assembly

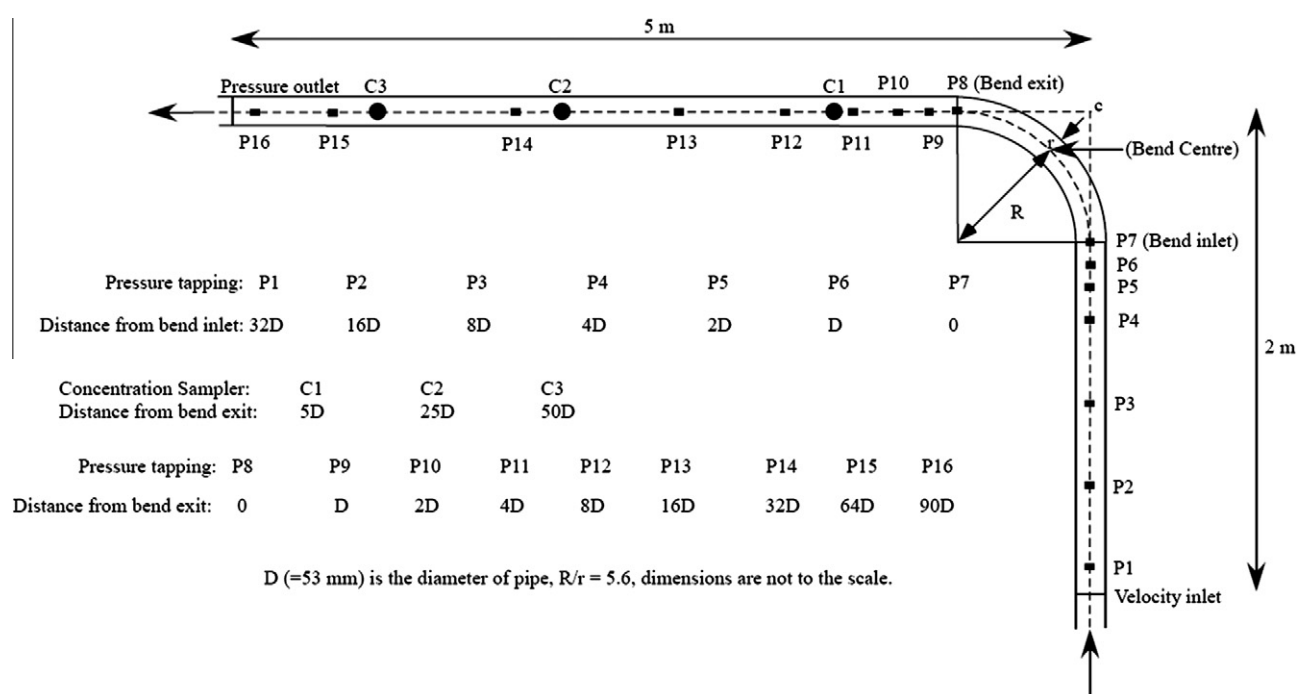


Fig. 2. Locations of pressure tappings and concentration samplers.

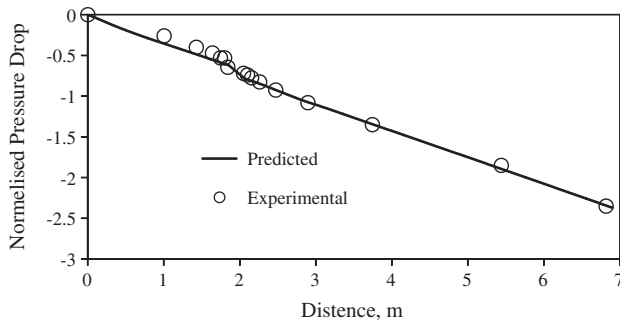


Fig. 4. Normalized pressure [$\Delta p / (\rho_w V_m^2 / 2)$] distributions for single-phase flow at $R/r = 5.6$ and $V_m = 3.56$ m/s.

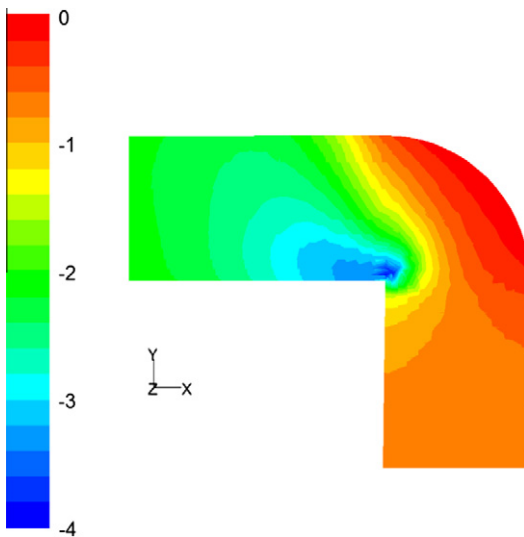


Fig. 5. Normalized pressure profiles [$\Delta p / (\rho_w V_m^2 / 2)$] for single-phase flow at $R/r = 0$ and $V_m = 3.56$ m/s.

is used in order that small pressure differences can be measured accurately. The pressure taps are provided with separation chambers to prevent blockage of the connecting tubes.

The concentration profiles are measured using concentration samplers C1, C2 and C3 located at 5D, 25D and 50D, respectively, in the downstream of bend exit as shown in Fig. 2. These concentration profiles are measured at mid-vertical plane (vertical diameter) of each cross-section by traversing the sampling tube from bottom to top of the pipe.

For continuous monitoring of the discharge by volume of slurry, a pre-calibrated electromagnetic flowmeter is installed in the vertical pipe section of the loop as shown in Fig. 1. Electromagnetic flow meter is calibrated by gravimetric method using measuring tank. The flow of slurry in the test loop is diverted to the measuring tank of 1.2 m^3 having a height of 1.5 m for known interval of time. The rise in the level of slurry in the tank for a given time interval was measured using a scale having a least count of 1 mm. The least count of the stop watch was 0.01 s. Flow rate by this method is evaluated with an accuracy of $\pm 0.5\%$. The similar procedure was repeated at various flow rates over the entire range of operation of the electromagnetic flow meter.

The test loop is also provided with an efflux sampling tube fitted with a plug valve in the vertical pipe section near the discharge end, for collection of the slurry sample to monitor the efflux concentration and density of the slurry.

The accuracy of a set of measurements is a function of the least count of the measuring instruments. In the present study, the

instruments used are manometer, electro-magnetic flowmeter and sampling probe. The resolution of manometer is ± 1 mm and ± 0.1 l/s for the electromagnetic flowmeter. The uncertainty in pressure drop measurements was determined by repeating experiments several times. The experimental data were found repeatable with errors due to uncertainty in measurements ranging between 1% and 3% depending upon the flow velocity. The stem size of sampling tube was 3 mm and sampling probe showed a variation of around 2% in concentration. The experimental loop has been checked for correct alignment between bend and straight pipe before taking each measurement.

3. Mathematical model

The use of a specific multiphase model (the discrete phase, mixture, Eulerian model) to characterize momentum transfer depends on the volume fraction of solid particles and on the fulfillment of the requirements which enable the selection of a given model. In practice, slurry flow through pipeline is not a diluted system, therefore the discrete phase model cannot be used to simulate its flow, but both the mixture model and the Eulerian model are appropriate in this case. Further, out of two versions of Eulerian model, granular version will be appropriate in the present case. The reason for choosing the granular in favor of the simpler non-granular multi-fluid model is that the non-granular model does not include models for taking friction and collisions between particles into account which is believed to be of importance in the slurry flow. The non-granular model also lacks possibilities to set a maximum packing limit which makes it less suitable for modeling flows with particulate secondary phase in the present case. Lun et al. (1984) and Gidaspow et al. (1992) proposed such a model for gas-solid flows. Slurry flow may be considered as gas-solid (pneumatic) flow by replacing the gas phase by water and maximum packing concentration by static settled concentration. Furthermore, few forces acting on solid phase may be prominent in case of slurry flow, which may be neglected in case of pneumatic flow. In the present study slurry pipeline bend is modeled using granular-Eulerian model as described below.

3.1. Eulerian model

Eulerian two-phase model assumes that the slurry flow consists of solid "s" and fluid "f" phases, which are separate, yet they form interpenetrating continua, so that $\alpha_f + \alpha_s = 1.0$, where α_f and α_s are the volumetric concentrations of fluid and solid phase, respectively. The laws for the conservation of mass and momentum are satisfied by each phase individually. Coupling is achieved by pressure and inter-phase exchange coefficients.

The forces acting on a single particle in the fluid are:

1. Static pressure gradient, ∇P .
2. Solid pressure gradient or the inertial force due to particle interactions, ∇P_s .
3. Drag force caused by the velocity difference between two phases, $K_{sf}(\vec{v}_s - \vec{v}_f)$, where, K_{sf} is the inter-phase drag coefficient, \vec{v}_s and \vec{v}_f are velocity of solid and fluid phase, respectively.
4. Viscous forces, $\nabla \cdot \bar{\tau}_f$, where, $\bar{\tau}_f$ is the stress tensor for fluid.
5. Body forces, ρg , where, ρ is the density and g is the acceleration due to gravity.
6. Virtual mass force as suggested by Drew and Lahey (1993), $C_{vm}\alpha_s\rho_f(\vec{v}_f \cdot \nabla \vec{v}_f - \vec{v}_s \cdot \nabla \vec{v}_s)$ where, C_{vm} is the coefficient of virtual mass force and is taken as 0.5 in the present study.
7. Lift force as suggested by Drew and Lahey (1993), $C_L\alpha_s\rho_f(\vec{v}_f - \vec{v}_s) \times (\nabla \times \vec{v}_f)$ where, C_L is the lift coefficient taken as 0.5 in the present study.

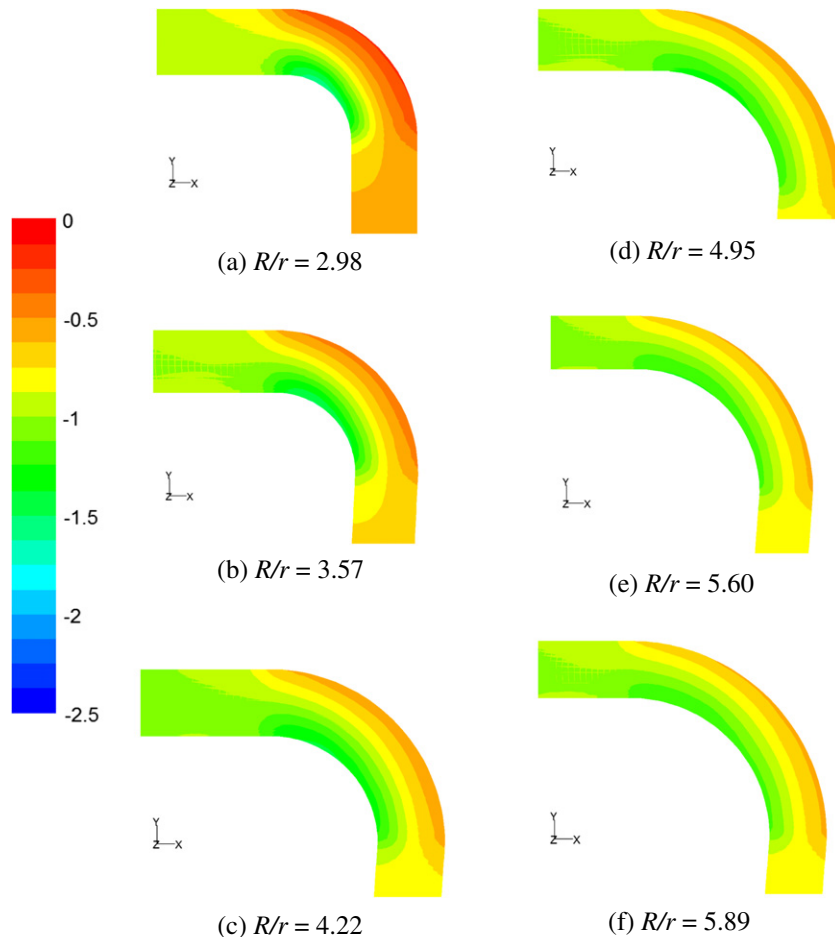


Fig. 6. Normalized pressure profiles $[\Delta p / (\rho_w V_m^2 / 2)]$ for single-phase flow at $R/r = 2.98\text{--}5.89$ and $V_m = 3.56 \text{ m/s}$.

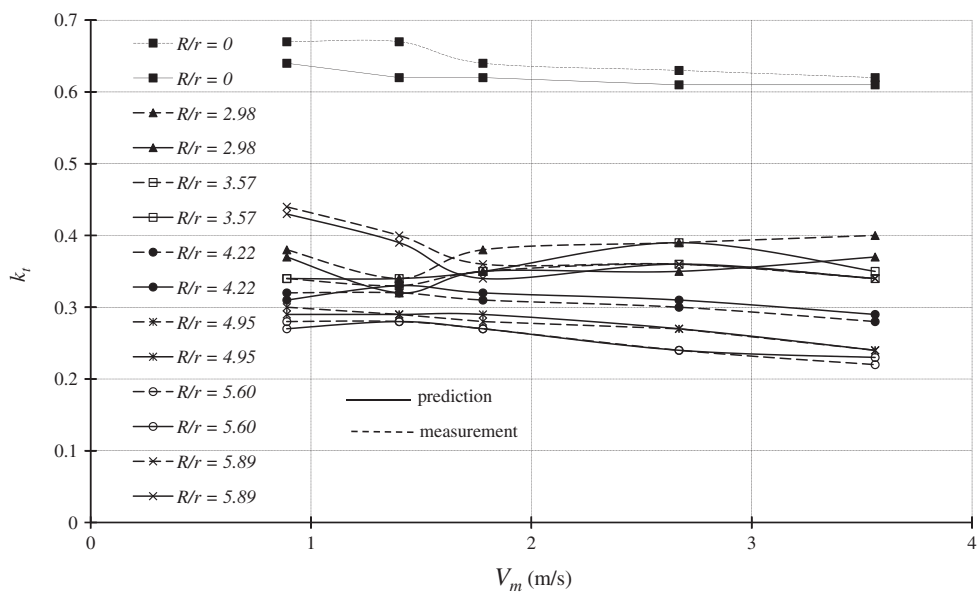


Fig. 7. Comparison between measured and predicted bend loss coefficient (k_t) for single-phase flow.

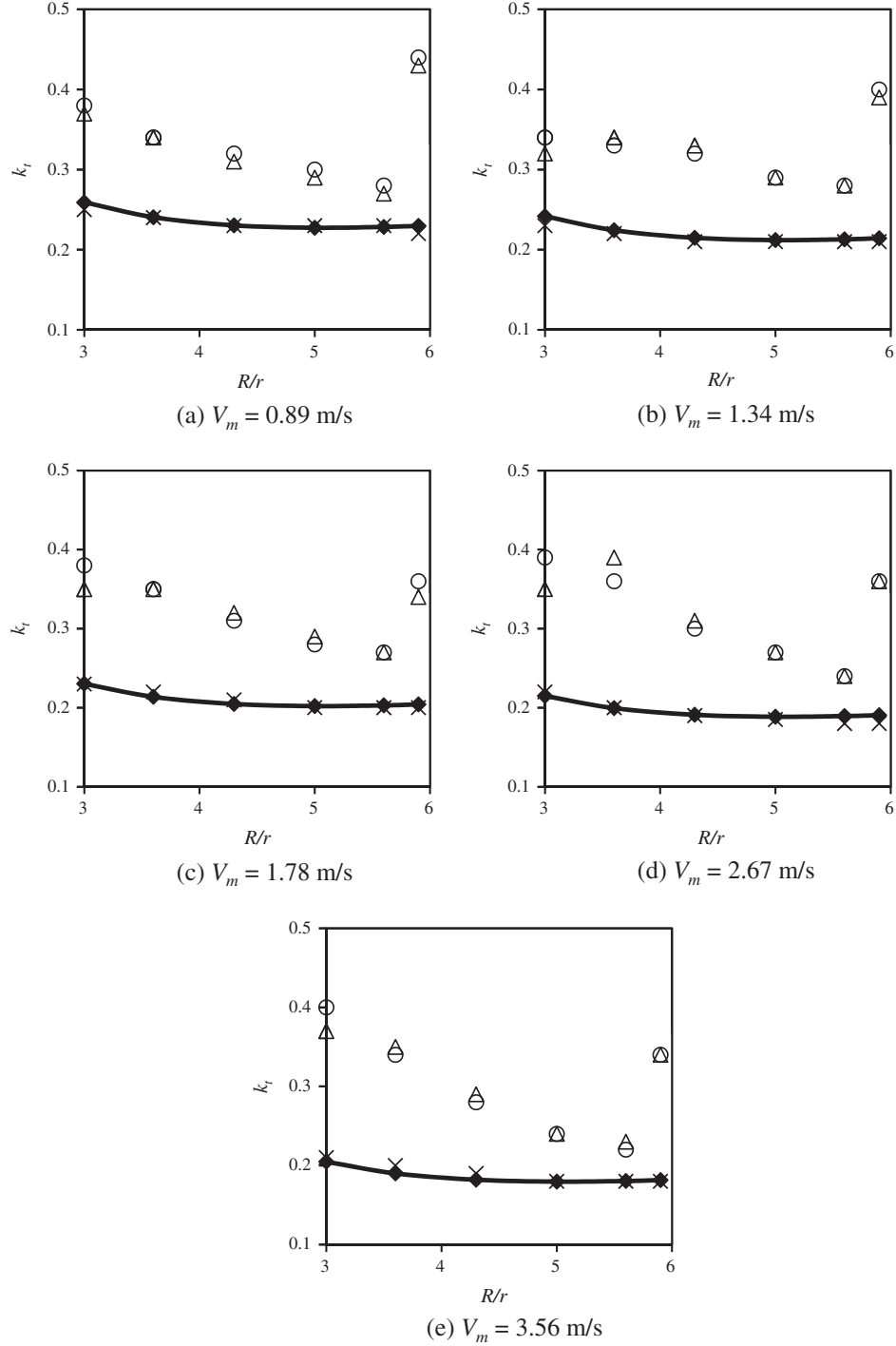


Fig. 8. Variation of bend loss coefficient (k_t) with R/r for single-phase flow (—♦— Ito (1960), $H_s/D = 0$; ◇ Measured, $H_s/D = 0.0003$ △ CFD, $H_s/D = 0.0003$; × CFD, $H_s/D = 0$).

3.1.1. Governing equations

3.1.1.1. Continuity equation.

$$\nabla \cdot (\alpha_t \rho_t \vec{v}_t) = 0$$

where t is either s or f .

3.1.1.2. Momentum equations. Momentum equation for fluid phase:

$$\begin{aligned} \nabla \cdot (\alpha_f \rho_f \vec{v}_f \vec{v}_f) &= -\alpha_f \nabla P + \nabla \cdot \bar{\tau}_f + \alpha_f \rho_f \vec{g} + K_{sf} (\vec{v}_s - \vec{v}_f) \\ &+ C_{vm} \alpha_f \rho_f (\vec{v}_s \cdot \nabla \vec{v}_s - \vec{v}_f \cdot \nabla \vec{v}_f) \\ &+ C_L \alpha_s \rho_f (\vec{v}_f - \vec{v}_s) \times (\nabla \times \vec{v}_f) \end{aligned} \quad (2)$$

Momentum equation for solid phase:

$$\begin{aligned} \nabla \cdot (\alpha_s \rho_s \vec{v}_s \vec{v}_s) &= -\alpha_s \nabla P - \nabla P_s + \nabla \cdot \bar{\tau}_s + \alpha_s \rho_f \vec{g} \\ &+ K_{fs} (\vec{v}_f - \vec{v}_s) \\ &+ C_{vm} \alpha_s \rho_f (\vec{v}_f \cdot \nabla \vec{v}_f - \vec{v}_s \cdot \nabla \vec{v}_s) \\ &+ C_L \alpha_s \rho_f (\vec{v}_s - \vec{v}_f) \times (\nabla \times \vec{v}_f) \end{aligned} \quad (3)$$

where $\bar{\tau}_s$ and $\bar{\tau}_f$ are the stress tensors for solid and fluid, respectively, which are expressed as

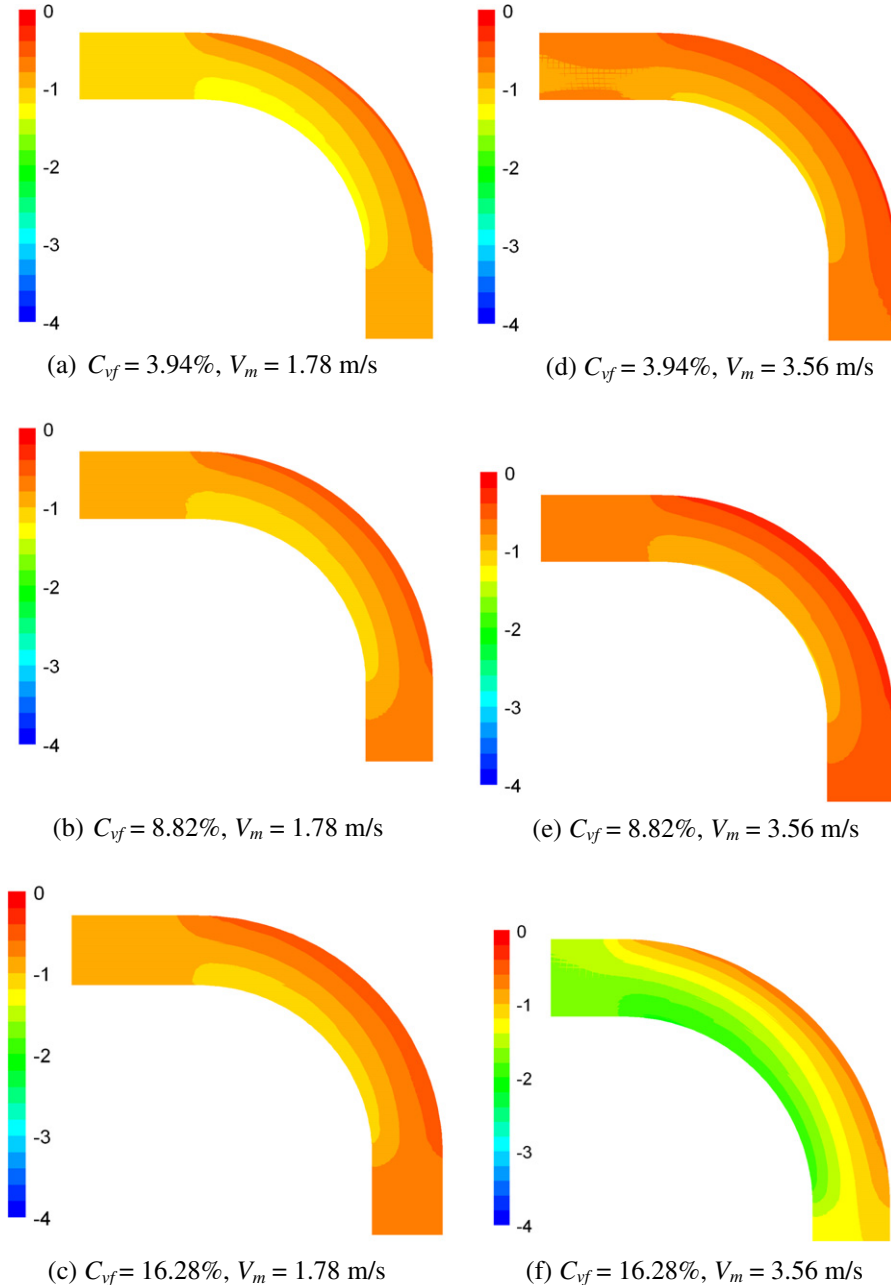


Fig. 9. Normalized pressure profiles $\left[\Delta p / (\rho_m V_m^2 / 2)\right]$ for slurry flow in pipe bend at mid-horizontal plane.

$$\bar{\tau}_s = \alpha_s \mu_s \left(\nabla \vec{v}_s + \nabla \vec{v}_s^{tr} \right) + \alpha_s \left(\lambda_s - \frac{2}{3} \mu_s \right) \nabla \cdot \vec{v}_s \bar{I} \quad (4)$$

and

$$\bar{\tau}_f = \alpha_f \mu_f \left(\nabla \vec{v}_f + \nabla \vec{v}_f^{tr} \right) \quad (5)$$

with superscript 'tr' over velocity vector indicating transpose. \bar{I} is the identity tensor. λ_s is the bulk viscosity of the solids as given by Lun et al. (1984):

$$\lambda_s = \frac{4}{3} \alpha_s \rho_s d_s g_{0,ss} \left(1 + e_{ss} \right) \left(\frac{\Theta_s}{\pi} \right)^{\frac{1}{3}} \quad (6)$$

d_s is the particle diameter put as 450 μm . $g_{0,ss}$ is the radial distribution function, which is interpreted as the probability of particle touching another particle, as given by Gidaspow et al. (1992):

$$g_{0,ss} = \left[1 - \left(\frac{\alpha_s}{\alpha_{s,\max}} \right)^{\frac{1}{3}} \right]^{-1} \quad (7)$$

$\alpha_{s,\max}$ is the static settled concentration measured experimentally 0.52. Θ_s is the granular temperature, which is proportional to the kinetic energy of the fluctuating particle motion and is modeled as described in Section 3.1.4. e_{ss} is the restitution coefficient, taken as 0.9 for silica sand particles. μ_f is the shear viscosity of fluid. μ_s is the shear viscosity of solids defined as

$$\mu_s = \mu_{s,col} + \mu_{s,kin} + \mu_{s,fr} \quad (8)$$

where $\mu_{s,col}$, $\mu_{s,fr}$ and $\mu_{s,kin}$ are collisional, frictional and kinetic viscosity are calculated using the expressions given by Gidaspow et al. (1992), Schaeffer (1987) and Syamlal et al. (1993), respectively, as given by:

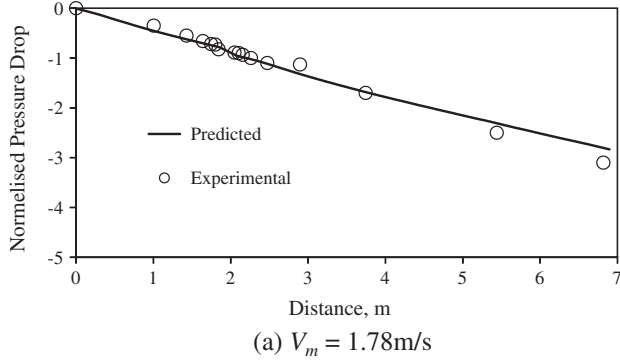
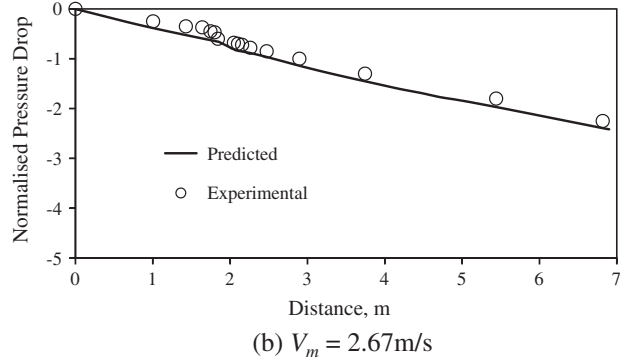
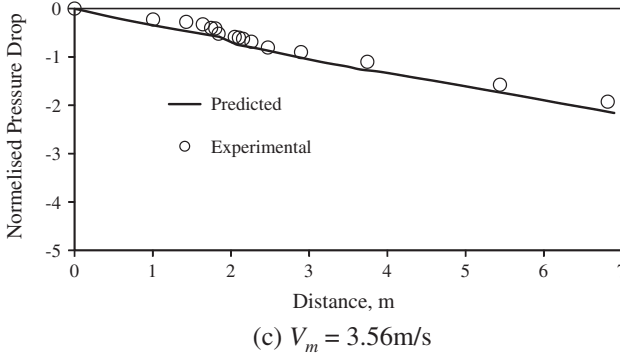
(a) $V_m = 1.78\text{m/s}$ (b) $V_m = 2.67\text{m/s}$ (c) $V_m = 3.56\text{m/s}$

Fig. 10. Normalized pressure drop $\left[\Delta p / \left(\rho_m V_m^2 / 2\right)\right]$ distribution at different V_m for $C_{vf} = 3.94\%$.

$$\mu_{s,col} = \frac{4}{5} \alpha_s \rho_s d_s g_{o,ss} (1 + e_{ss}) \left(\frac{\Theta_s}{\pi} \right)^{\frac{1}{2}}, \quad (9)$$

$$\mu_{s,fr} = \frac{P_s \sin \phi}{2 \sqrt{I_{2D}}}, \quad (10)$$

and

$$\mu_{s,kin} = \mu_{s,kin} = \frac{\alpha_s d_s \rho_s \sqrt{\Theta_s \pi}}{6(3 - e_{ss})} \left[1 + \frac{2}{5} (1 + e_{ss}) (3e_{ss} - 1) \alpha_s g_{o,ss} \right] \quad (11)$$

I_{2D} is the second invariant of the strain rate tensor. P_s is the solid pressure as given by Lun et al. (1984):

$$P_s = \alpha_s \rho_s \Theta_s + 2 \rho_s (1 + e_{ss}) \alpha_s g_{o,ss} \Theta_s \quad (12)$$

ϕ is the internal friction angle taken as 30° in the present computations. $K_{sf}(=K_{fs})$ is the inter-phase momentum exchange coefficient given by Syamlal et al. (1993):

$$K_{sf} = K_{fs} = \frac{3}{4} \frac{\alpha_s \alpha_f \rho_f}{V_{r,s}^2 d_s} C_D \left(\frac{Re_s}{V_{r,s}} \right) |\vec{v}_s - \vec{v}_f| \quad (13)$$

C_D is the drag coefficient given by Richardson and Zaki (1954):

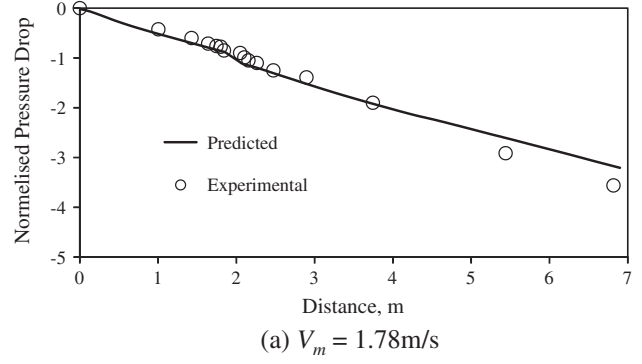
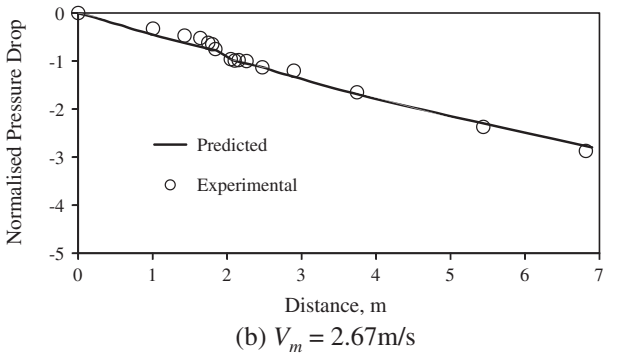
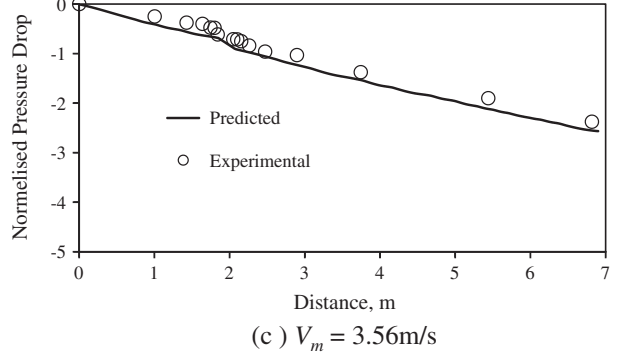
(a) $V_m = 1.78\text{m/s}$ (b) $V_m = 2.67\text{m/s}$ (c) $V_m = 3.56\text{m/s}$

Fig. 11. Normalized pressure drop $\left[\Delta p / \left(\rho_m V_m^2 / 2\right)\right]$ distribution at different V_m for $C_{vf} = 8.82\%$.

$$C_D = \left[0.63 + 4.8 \left(\frac{Re_s}{V_{r,s}} \right)^{-\frac{1}{2}} \right]^2 \quad (14)$$

Re_s is the relative Reynolds number given by

$$Re_s = \frac{\rho_f d_s |\vec{v}_s - \vec{v}_f|}{\mu_f} \quad (15)$$

$V_{r,s}$ is the terminal velocity correlation for solid phase as given by Garside and Al-Dibouni (1977):

$$V_{r,s} = 0.5 \left(A - 0.06 Re_s + \sqrt{(0.06 Re_s)^2 + 0.12 Re_s (2B - A) + A^2} \right) \quad (16)$$

with

$$A = \alpha_f^{4.14}; \quad B = 0.8 \alpha_f^{1.28} \quad \text{for } \alpha_f \leq 0.85 \quad (17)$$

and

$$A = \alpha_f^{4.14}; \quad B = \alpha_f^{2.65} \quad \text{for } \alpha_f > 0.85 \quad (18)$$

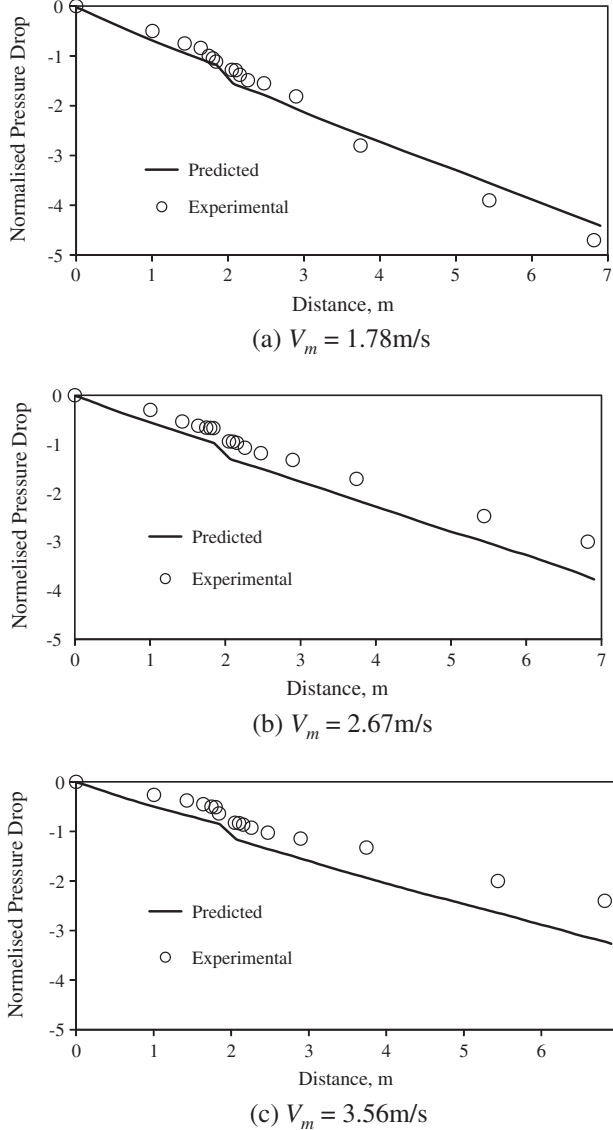


Fig. 12. Normalized pressure drop $[\Delta p / (\rho_m V_m^2 / 2)]$ distribution at different V_m for $C_{vf} = 16.28\%$.

3.1.2. Turbulence closure for the fluid phase

Predictions for turbulent quantities for the fluid phase are obtained using standard $k-\varepsilon$ model (Launder and Spalding, 1974) supplemented by additional terms that take into account inter-phase turbulent momentum transfer.

The Reynolds stress tensor for the fluid phase is

$$\overline{\tau_{tf}} = -\frac{2}{3}(\rho_f k_f + \mu_{tf} \nabla \vec{v}_f) \bar{I} + \mu_{tf} (\nabla \vec{v}_f + \nabla \vec{v}_f^T) \quad (19)$$

where μ_{tf} is the turbulent viscosity given by

$$\mu_{tf} = \rho_f C_\mu \frac{k_f^2}{\varepsilon_f} \quad \text{with } C_\mu = 0.09 \quad (20)$$

The predictions of turbulent kinetic energy k_f and its rate of dissipation ε_f are obtained from following transport equations

$$\nabla \cdot (\alpha_f \rho_f \overline{U_f} k_f) = \nabla \cdot \left(\alpha_f \frac{\mu_{tf}}{\sigma_k} \nabla k_f \right) + \alpha_f G_{kf} - \alpha_f \rho_f \varepsilon_f + \alpha_f \rho_f \prod_{kf} \quad (21)$$

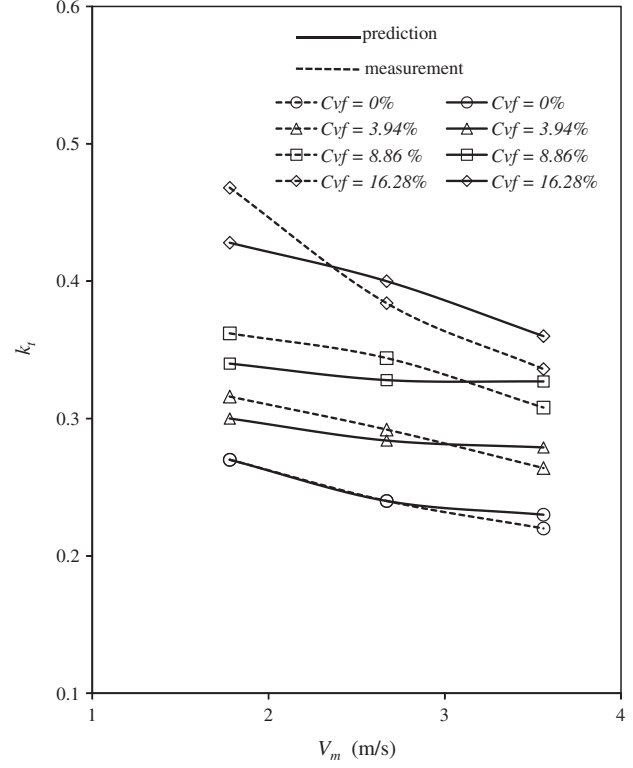


Fig. 13. Comparison between measured and predicted bend loss coefficient (k_r) in slurry flow for $R/r = 5.6$.

$$\begin{aligned} \nabla \cdot (\alpha_f \rho_f \overline{U_f} \varepsilon_f) &= \nabla \cdot \left(\alpha_f \frac{\mu_{tf}}{\sigma_\varepsilon} \nabla \varepsilon_f \right) + \alpha_f \\ &\times \frac{\varepsilon_f}{k_f} (C_{1\varepsilon} G_{kf} - C_{2\varepsilon} \rho_f \varepsilon_f) + \alpha_f \rho_f \prod_{ef} \end{aligned} \quad (22)$$

where \prod_{kf} and \prod_{ef} represent the influence of the solid phase on the fluid phase given by

$$\prod_{kf} = \frac{K_{sf}}{\alpha_f \rho_f} (k_{sf} - 2k_f + \overrightarrow{v_{sf}} \cdot \overrightarrow{v_{dr}}) \quad (23)$$

$$\prod_{ef} = C_{3\varepsilon} \frac{\varepsilon_f}{k_f} \prod_{kf} \quad (24)$$

$\overrightarrow{v_{dr}}$ is the drift velocity given by

$$\overrightarrow{v_{dr}} = \left(\frac{D_s}{\sigma_{sf} \alpha_s} \nabla \alpha_s - \frac{\mu_{tf}}{\sigma_{sf} \alpha_f} \nabla \alpha_f \right) \quad (25)$$

$\overrightarrow{v_{sf}}$ is the slip-velocity, the relative velocity between fluid phase and solid phase given by

$$\overrightarrow{v_{sf}} = \overrightarrow{v_s} - \overrightarrow{v_f} \quad (26)$$

D_s is the eddy viscosity for solid phase is defined in the next section. σ_{sf} is a constant taken as 0.75. k_{sf} is the co-variance of the velocity of fluid phase and solid phase defined as average of product of fluid and solid velocity fluctuations. G_{kf} is the production of the turbulent kinetic energy in the flow defined as the rate of kinetic energy removed from the mean and organized motions by the Reynolds stresses given by

$$G_{kf} = \mu_{tf} (\nabla \vec{v}_f + \nabla \vec{v}_f^T) : \nabla \vec{v}_f \quad (27)$$

The constant parameters used in different equations are taken as

$$C_{1\varepsilon} = 1.44, \quad C_{2\varepsilon} = 1.92, \quad C_{3\varepsilon} = 1.2, \quad \sigma_k = 1.0, \quad \sigma_\varepsilon = 1.3$$

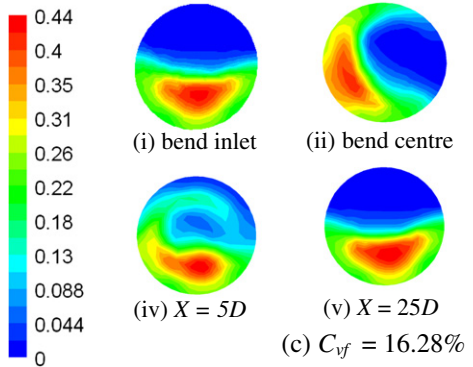
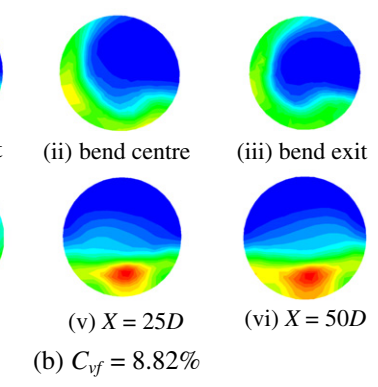
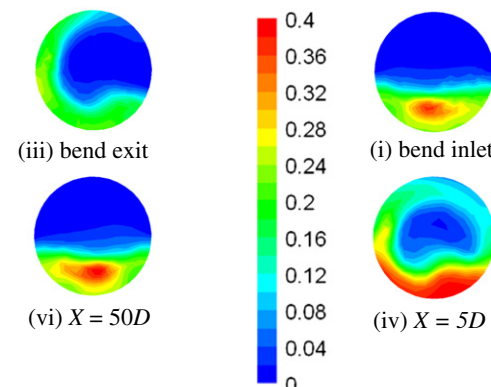
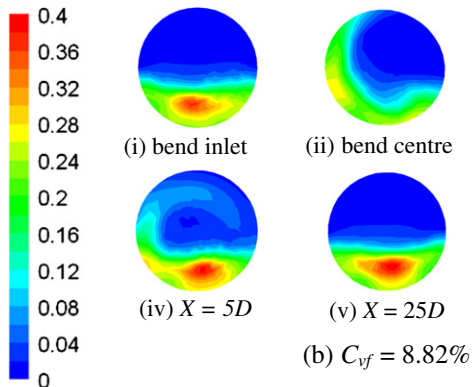
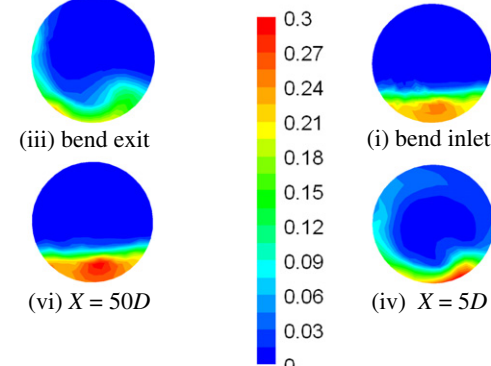
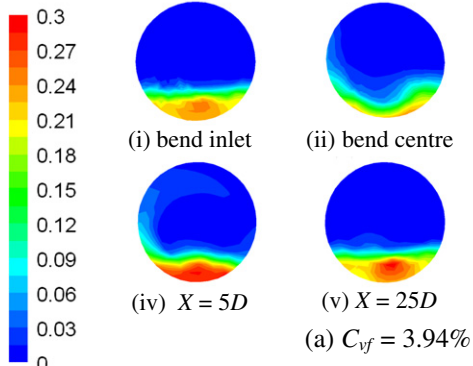


Fig. 14. Cross-sectional concentration (α_s) distribution at different locations from the bend exit at different concentrations for $V_m = 1.78$ m/s at $R/r = 5.6$.

3.1.3. Turbulence in the solid phase

To predict turbulence in solid phase, Tchen's theory (Lun et al., 1984) of the dispersion of discrete particle in homogeneous and steady turbulent flow is used. Dispersion coefficients, correlation functions, and turbulent kinetic energy of the solid phase are represented in terms of the characteristics of continuous turbulent motions of fluid phase based on two time scales. The first time scale considering inertial effects acting on the particle:

$$\tau_{F,sf} = \alpha_s \rho_f K_{sf}^{-1} \left(\frac{\rho_s}{\rho_f} + C_{vm} \right) \quad (28)$$

The second characteristic time of correlated turbulent motion or eddy-particle interaction time:

$$\tau_{t,sf} = \tau_{t,f} [1 + C_\beta \xi^2]^{-\frac{1}{2}} \quad (29)$$

$$\xi = \frac{|\vec{V}_r|}{\sqrt{\frac{2}{3}} k_f} \quad (30)$$

Fig. 15. Cross-sectional concentration (α_s) distribution at different locations from the bend exit at different concentrations for $V_m = 2.67$ m/s at $R/r = 5.6$.

The characteristic time of energetic turbulent eddies:

$$\tau_{t,f} = \frac{3}{2} C_\mu \frac{k_f}{\varepsilon_f} \quad (31)$$

$|\vec{V}_r|$ is the average value of the local relative velocity between particle and surrounding fluid defined as the difference in slip and drift velocity ($\vec{V}_r = \vec{v}_{sf} - \vec{v}_{dr}$).

$$C_\beta = 1.8 - 1.35 \cos^2 \theta \quad (32)$$

θ is the angle between the mean particle velocity and mean relative velocity.

η_{sf} is the ratio between two characteristic times given by

$$\eta_{sf} = \frac{\tau_{t,sf}}{\tau_{F,sf}} \quad (33)$$

k_s is the turbulent kinetic energy of the solid phase given by

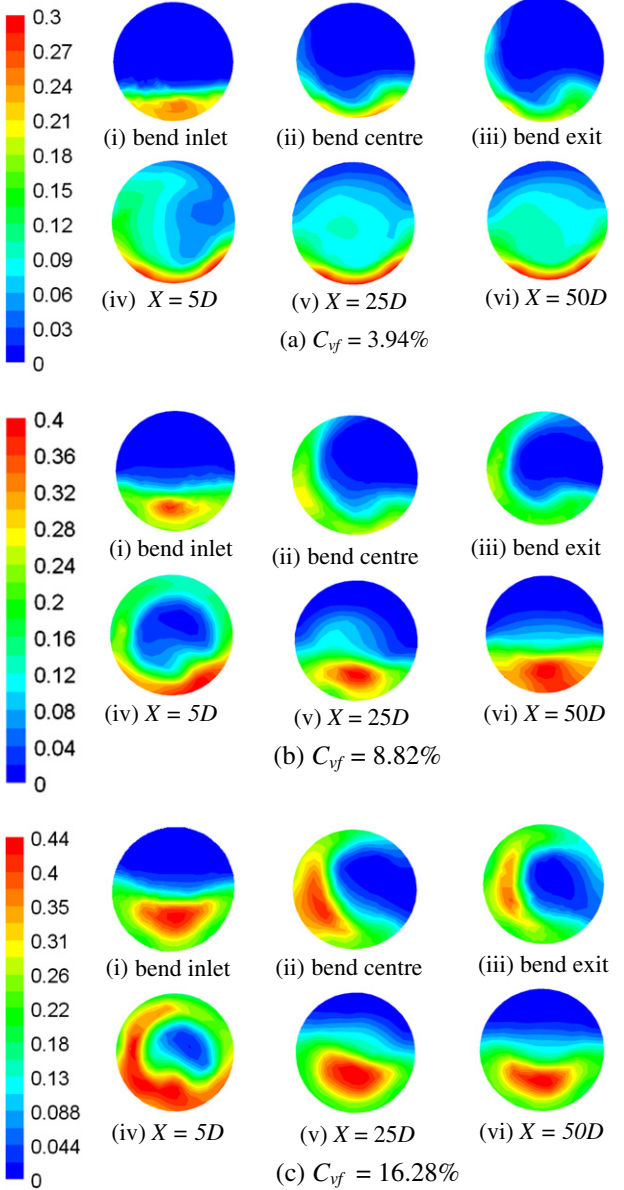


Fig. 16. Cross-sectional concentration (α_s) distribution at different locations from the bend exit at different concentrations for $V_m = 3.56$ m/s at $R/r = 5.6$.

$$k_s = k_f \left(\frac{b^2 + \eta_{sf}}{1 + \eta_{sf}} \right) \quad (34)$$

D_s is the eddy viscosity for the solid phase given by

$$D_s = D_{t,sf} + \left(\frac{2}{3} k_s - b \frac{1}{3} k_{sf} \right) \tau_{F,sf} \quad (35)$$

$D_{t,sf}$ is the binary turbulent diffusion coefficient given by

$$D_{t,sf} = \frac{1}{3} k_{sf} \tau_{t,sf} \quad (36)$$

with

$$b = (1 + C_{Vm}) \left(\frac{\rho_s}{\rho_f} + C_{Vm} \right)^{-1} \quad (37)$$

3.1.4. Transport equation for granular temperature (Θ_s)

The granular temperature for solid phase describes the kinetic energy of random motion of solid particles. The transport equation

derived from the kinetic theory (Ding and Gidaspow, 1990) takes the following form:

$$\begin{aligned} \frac{3}{2} \nabla \cdot (\rho_s \alpha_s \vec{v}_s \Theta_s) &= (-P_s \bar{I} + \bar{\tau}_s) \\ &+ \nabla \vec{v}_s + \nabla \cdot (k_{\Theta_s} \nabla \Theta_s) - \gamma_{\Theta_s} + \varphi_{fs} \end{aligned} \quad (38)$$

where the term $(-P_s \bar{I} + \bar{\tau}_s) : \nabla \vec{v}_s$ is defined as the generation of energy by the solid stress tensor. k_{Θ_s} is the diffusion coefficient as given by Syamlal et al. (1993):

$$k_{\Theta_s} = \frac{15 d_s \rho_s \alpha_s \sqrt{\Theta_s \pi}}{4(41-33\eta)} \left[1 + \frac{12}{5} \eta^2 (4\eta-3) \alpha_s g_{0,ss} + \frac{16}{15\pi} (41-33\eta) \eta \alpha_s g_{0,ss} \right] \quad (39)$$

where

$$\eta = \frac{1}{2} (1 + e_{ss}) \quad (40)$$

Further, γ_{Θ_s} is the collisional dissipation energy, which represents the energy dissipation rate within the solid phase due to collision between particles as given by Lun et al. (1984):

$$\gamma_{\Theta_s} = \frac{12(1-e_{ss}^2)g_{0,ss}}{d_s \sqrt{\pi}} \rho_s \alpha_s^2 \Theta_s^{3/2} \quad (41)$$

φ_{fs} is the transfer of the kinetic energy of random fluctuation in particle velocity from solid phase to the fluid as given by Gidaspow et al. (1992):

$$\varphi_{fs} = -3K_{fs} \Theta_s \quad (42)$$

3.2. Wall function

In the region near the wall, the gradient of quantities is high and requires fine grids. This causes the calculation to become more expensive, meaning time-consuming, requiring greater memory and faster processing on the computer, as well as expensive in terms of the complexity of equations. A wall function, which is a collection of semiempirical formulas and functions, provides a cheaper calculation by substituting the fine grids with a set of equations linking the calculated variables at near-wall cells and the corresponding quantities on the wall. The wall function helps in more precise calculation of near-wall shear stresses for both liquid and solid phases.

A no-slip condition is applied to the liquid phase at the wall surface, with wall roughness height (H_s) of 0.015 mm. A modified wall function is used to account for roughness for liquid phase (water):

$$\frac{0.548 v_{fp} k^{1/2}}{\tau_{fw}/\rho_f} = \frac{1}{0.42} \ln \left(5.373 \frac{\rho_f z_p k^{1/2}}{\mu_f} \right) - \Delta B \quad (43)$$

where v_{fp} and z_p are the mean velocity and the distance from the wall, respectively, k is the kinetic energy, ρ_f is the density, μ_f is the viscosity and τ_{fw} is the wall shear stress for water. The roughness function ΔB is based on the formulas proposed by Cebeci and Bradshaw (1977), and its computation depends on the roughness regime (H_s^+):

$$H_s^+ = 0.548 \rho \frac{H_s k^{1/2}}{\mu}$$

For $H_s^+ < 3$, $\Delta B = 0$

For $3 < H_s^+ < 70$

$$\Delta B = \frac{1}{0.42} \left[\frac{H_s^+ - 2.25}{87.75} + 0.5H_s^+ \right] \cdot \sin \{ 0.4258(\ln H_s^+ - 0.811) \} \quad (44)$$

$$\text{For } H_s^+ > 70, \Delta B = \frac{1}{0.42} \ln (1 + 0.5H_s^+)$$

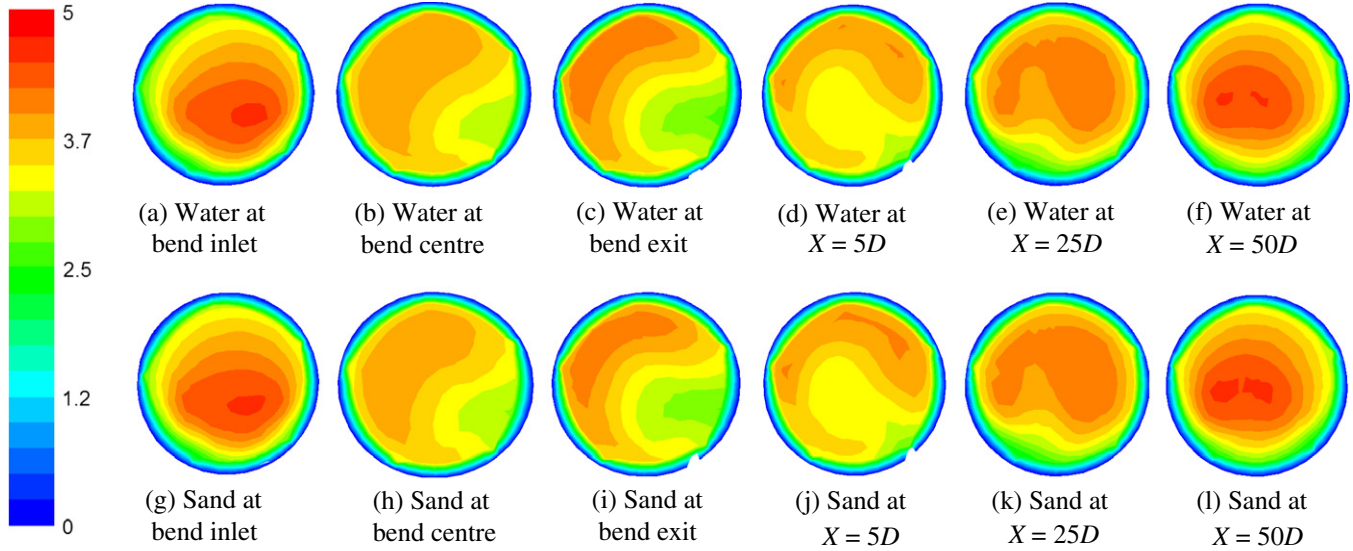


Fig. 17. Distributions of v_{fz} and v_{sz} in m/s at $C_{vf} = 8.82\%$ and $V_m = 3.56$ m/s.

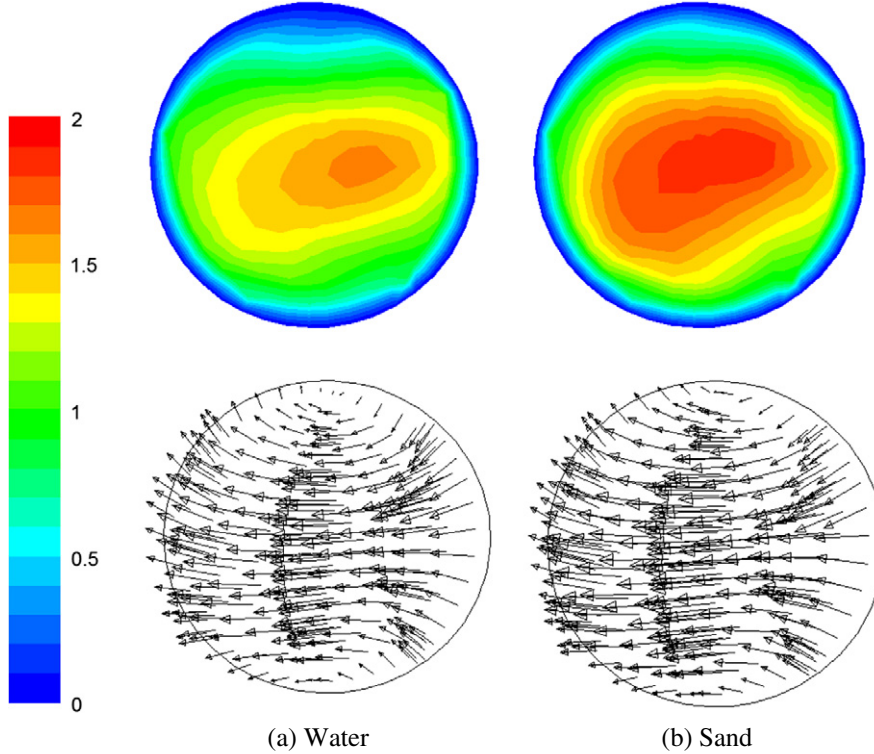


Fig. 18. Contours of magnitude and directions of velocity component in the plane perpendicular to the direction of flow in m/s for $C_{vf} = 8.82\%$ and $V_m = 3.56$ m/s at bend centre.

In the FLUENT (2006) solver, ΔB is evaluated using the corresponding formula in Eq. (44). The modified law of the wall in Eq. (43) is then used to evaluate the shear stress at the wall and other wall functions for the turbulent quantities for water.

For solid phase (silica sand), the semi-empirical equations developed by Johnson and Jackson (1987), expressed as Eqs. (45) and (46) are used to calculate the solid tangential velocity and granular temperature at wall. Specularity coefficient ϕ_w represents the tangential momentum loss in the particle–wall collisions, and high granular energy will be produced at the high specularity coefficient. The investigations of slurry flows show that it is difficult to measure the specularity coefficient ϕ_w and the parti-

cle–wall restitution coefficient e_w in the experiment, so the appropriate values for a specified flow system are generally determined by sensitivity analysis in the numerical investigations (Benyahia et al., 2007).

$$\vec{v}_{s,w} = - \frac{6\mu_s \alpha_{s,max}}{\sqrt{3}\pi\phi_w \rho_s g_{0,ss} \sqrt{\Theta_{s,w}}} \frac{\partial \vec{v}_{s,w}}{\partial n} \quad (45)$$

$$\Theta_{s,w} = - \frac{\kappa_{\theta,s,w}}{\gamma_w} \frac{\partial \Theta_{s,w}}{\partial n} + \frac{\sqrt{3}\pi\phi_w \rho_s \alpha_s \vec{v}_{s,w}^2 g_{0,ss} \Theta_{s,w}^{3/2}}{6\alpha_{s,max} \gamma_w} \quad (46)$$

where $\gamma_w = \frac{\sqrt{3}\pi(1-e_w^2)\alpha_s \rho_s g_{0,ss} \Theta_{s,w}^{3/2}}{4\alpha_{s,max}}$.

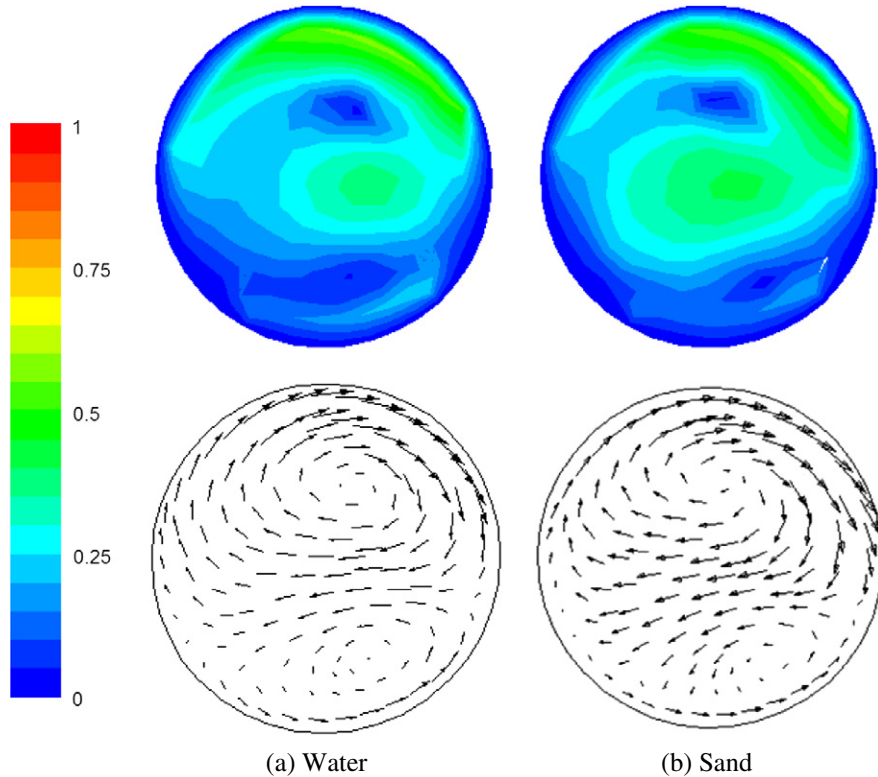


Fig. 19. Contours of magnitude and directions of velocity component in the plane perpendicular to the direction of flow in m/s for $C_{vf} = 8.82\%$ and $V_m = 3.56$ m/s at bend exit.

The parameters used in the model are determined referring to the previous numerical and experimental studies on slurry flows with the same type of particles. The particle-wall restitution coefficient e_w is taken as 0.99 and the specularity coefficient

ϕ_w used in the Johnson-Jackson wall boundary conditions is 0.0001, namely only 0.01% of tangential momentum is lost after the particle-wall collisions (Benyahia et al., 2007; Pain et al., 2001).

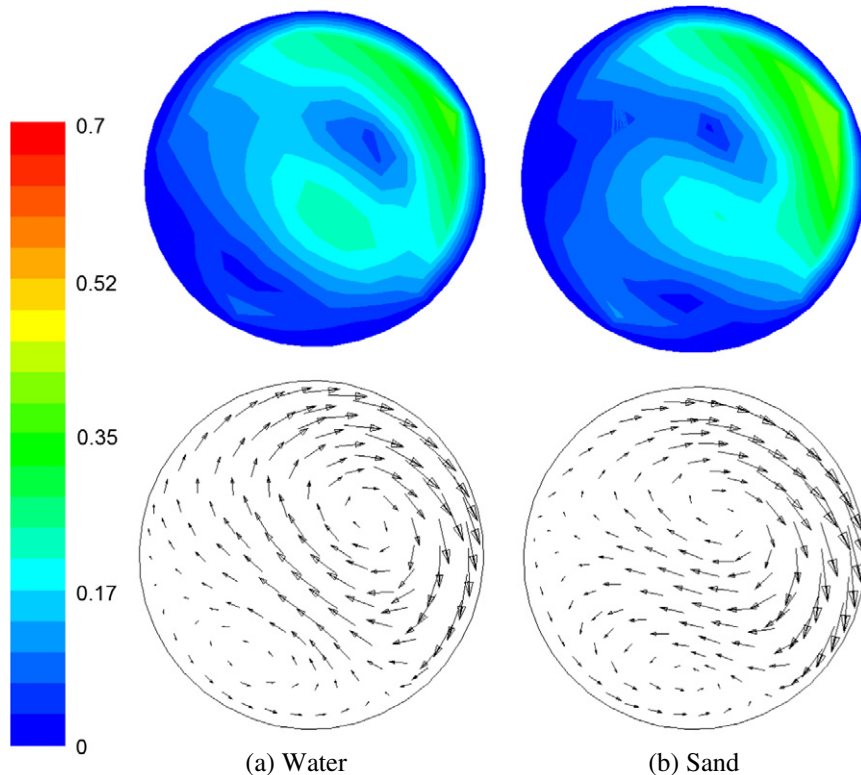


Fig. 20. Contours of magnitude and directions of velocity component in the plane perpendicular to the direction of flow in m/s for $C_{vf} = 8.82\%$ and $V_m = 3.56$ m/s at $X = 5D$.

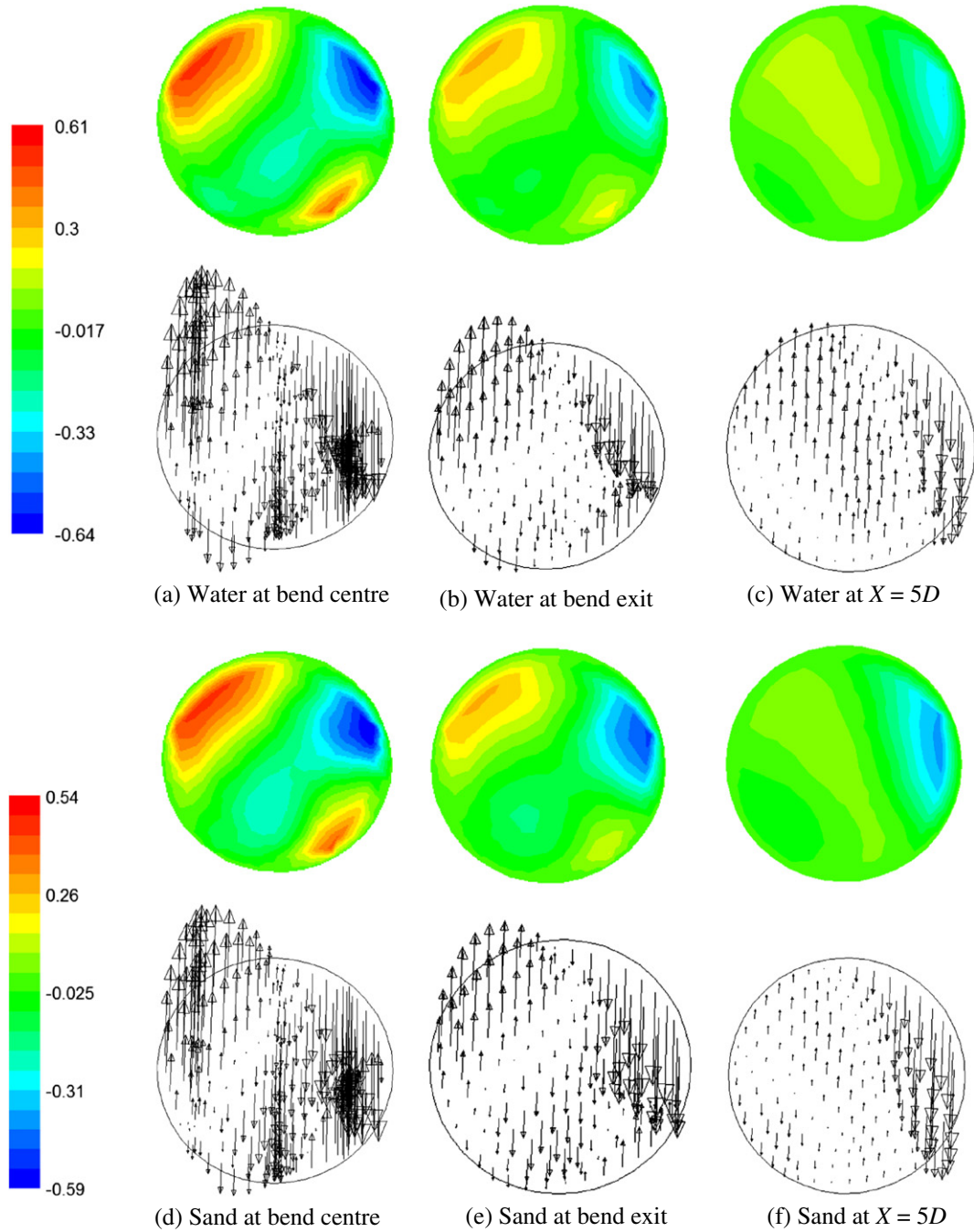


Fig. 21. Contours of magnitude and directions of vertical velocities $v_{fz}(x, y)$ and $v_{sz}(x, y)$ in m/s for $C_{vf} = 8.82\%$ and $V_m = 3.56$ m/s.

Centrifugal force due to presence of bend gets calculated automatically by FLUENT based on the development of radial pressure gradient due to curved streamlines along the bend section.

4. Numerical solution

4.1. Geometry

In single phase flow it is well established that an entrance length of $30D$ to $50D$ is necessary to establish fully developed turbulent pipe flow. Whilst such estimates were used as a guide, a series of numerical trials were conducted using different pipe lengths. For all of the cases simulated here, a pipe length of $32D$

was sufficient to give a fully developed slurry flow at the upstream of bend inlet. Using a longer pipe did not affect the results. In view of this, the reference pressure is chosen $32D$ upstream of the bend inlet. As the present study is focussed on analyzing the slurry-flow behavior in 90° horizontal bend only, there is no use of taking reference point at distance larger than $32D$. Velocity inlet is kept 15 cm upstream of reference point which is at $32D$ upstream of the bend inlet (Fig. 2). The bend is laid horizontally in (x, y) plane with origin $(0, 0, 0)$ at centre of velocity inlet. The direction of flow at velocity inlet is in positive- y direction. The direction of flow at pressure outlet is in negative- x direction. The mid-vertical plane is in the z -axis intersecting pipe cross-section at the centre. The mid-horizontal plane is along the x and y -axis in (x, y) plane at

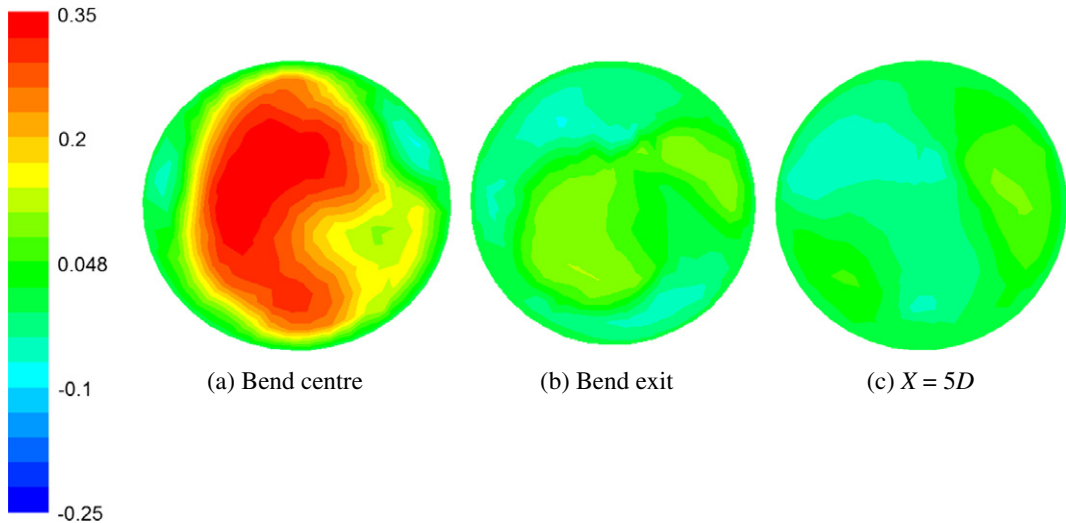


Fig. 22. Contours of slip velocity ($v_{sz} - v_{fx}$) in the plane perpendicular to the direction of flow in m/s for $C_{vf} = 8.82\%$ and $V_m = 3.56$ m/s.

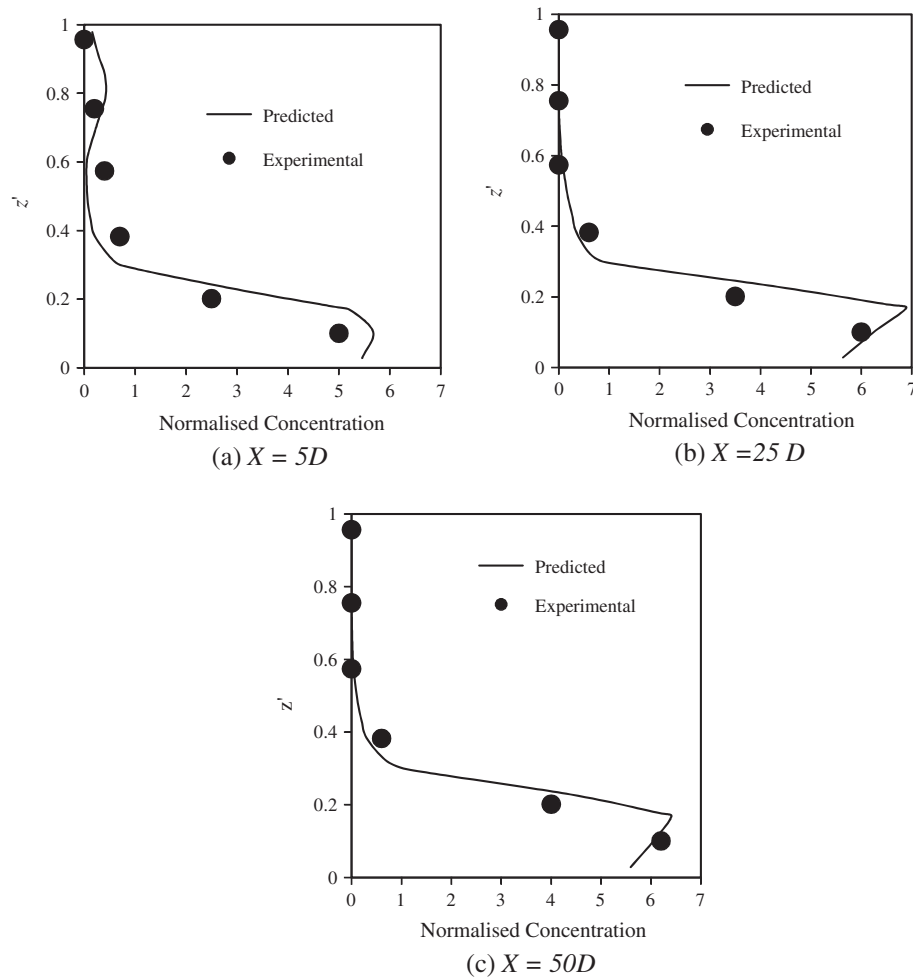


Fig. 23. Comparison between measured and predicted mid-vertical concentration profiles at different locations in the downstream of bend exit at $C_{vf} = 3.94\%$ and $V_m = 1.78$ m/s (Normalized concentration = $\alpha_s(z')/C_{vf}$).

velocity inlet and pressure outlet, respectively, intersecting pipe cross-section at the centre.

The computational grid for the bend similar to that used in experiments consisting of 266,670 cells and 303,456 nodes (Figs. 2 and 3)

has been generated using GAMBIT software. This number was generated by applying the same cross-sectional meshes obtained from the optimum cross-sectional meshes of pipe for the single-phase flow. The grid-independence tests were carried out keeping all the solver

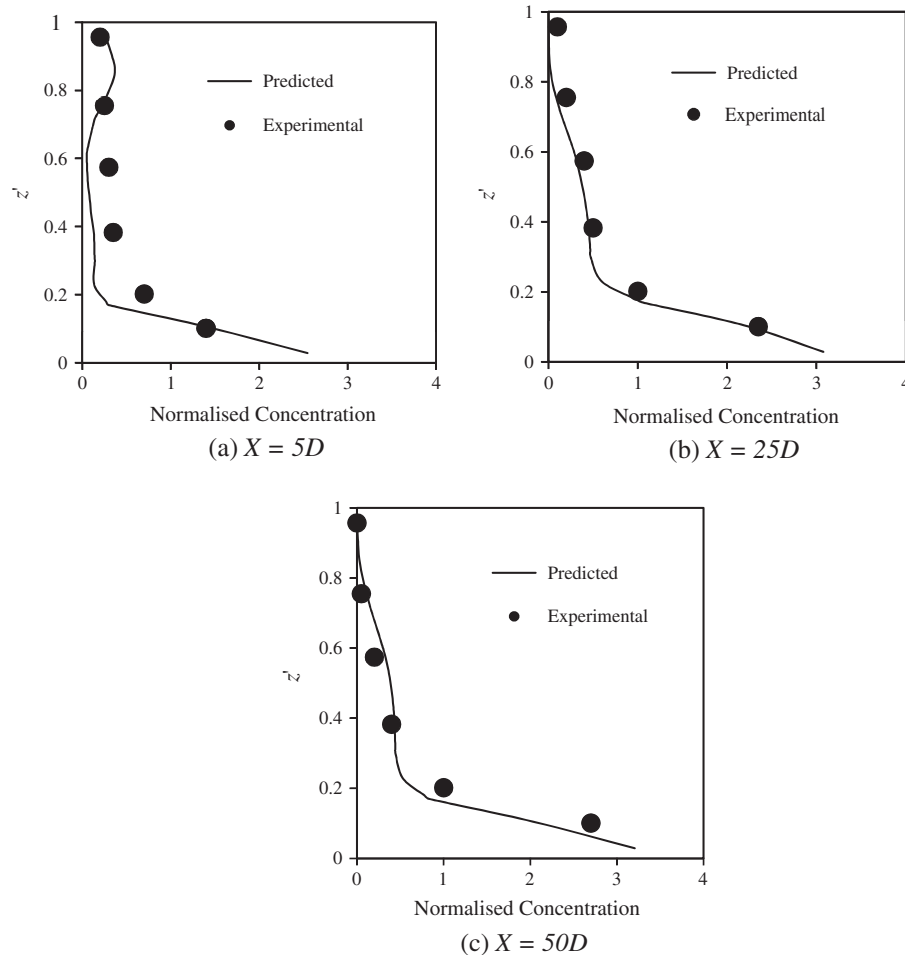


Fig. 24. Comparison between measured and predicted mid-vertical concentration profiles at different locations in the downstream of bend exit at $C_{vf} = 3.94\%$ and $V_m = 2.67 \text{ m/s}$ (Normalized concentration = $\alpha_s(z')/C_{vf}$).

parameters same for each simulation case. The grid independence tests consisted of refining the initial grid by approximately doubling the number of cells present in the initial grid. Hence, a grid size of 133,335 cells was first refined to 266,670 cells and then to 533,340 cells, for the pipe bend. There was no further improvement found in simulation results, when cells increased from 266,670 to 533,340. Therefore mesh containing 266,670 cells is optimum and is appropriate for simulation of the experimental data.

A boundary layer, which contains four cells with a distance of the cell adjacent to the wall at 5% of the diameter of the pipe and a growth factor of 1.2 was employed on the wall to improve the performance of the wall function and to fulfill the requirement of $z^+ \left(= \frac{\rho_f z_p k^{1/2}}{\mu_f}\right)$ for single-phase flow. It is essential to make sure that the depth of the wall-adjacent cells falls within the distance over which the log-law is valid ($30 < z^+ < 60$). The z^+ values for the pipe bend section in the present study vary as $41.5 \leq z^+ \leq 52.6$ for single-phase flow.

To obtain better convergence and accuracy for a long pipe, the hexagonal shape and Cooper type non-uniform three-dimensional grid has been employed. The Cooper type element is a volume meshing type in GAMBIT, which uses an algorithm to sweep the mesh node patterns of specified “source” faces through the volume.

4.2. Boundary conditions

There are three boundaries of the calculation domain (Fig. 2): the velocity inlet, the wall boundary and the pressure outlet. Fully

developed velocity and volume fraction profiles across the pipe cross-section for liquid and solid phases were introduced as the inlet condition of the bend. Fully developed velocity and volume fraction profiles across the pipe cross-section are computed at the outlet of 3 m long straight horizontal pipe having similar grid structure as described earlier for the bend.

Normalized concentration is defined as $\frac{\alpha_s(z')}{C_{vf}}$, where $z' = z/D_z$ is the height from pipe bottom along the vertical diameter of the cross-section. C_{vf} is calculated using following equation:

$$C_{vf} = \frac{1}{A} \int_A \alpha_s dA \quad (47)$$

4.3. Solution strategy and convergence

A second order upwind discretization scheme was used for the momentum equation while a first order upwind discretization was used for volume fraction, turbulent kinetic energy and turbulent energy dissipation. These schemes ensured satisfactory accuracy, stability and convergence.

The convergence criterion is based on the residual value of the calculated variables, i.e., mass, velocity components, turbulent kinetic energy, turbulent energy dissipation rate and volume fraction. In the present calculations, the residual value for convergence was set to a thousandth of the initial residual value of each variable. In pressure–velocity coupling, the phase coupled SIMPLE algorithm was used, which is an extension of the SIMPLE algorithm to multiphase flows.

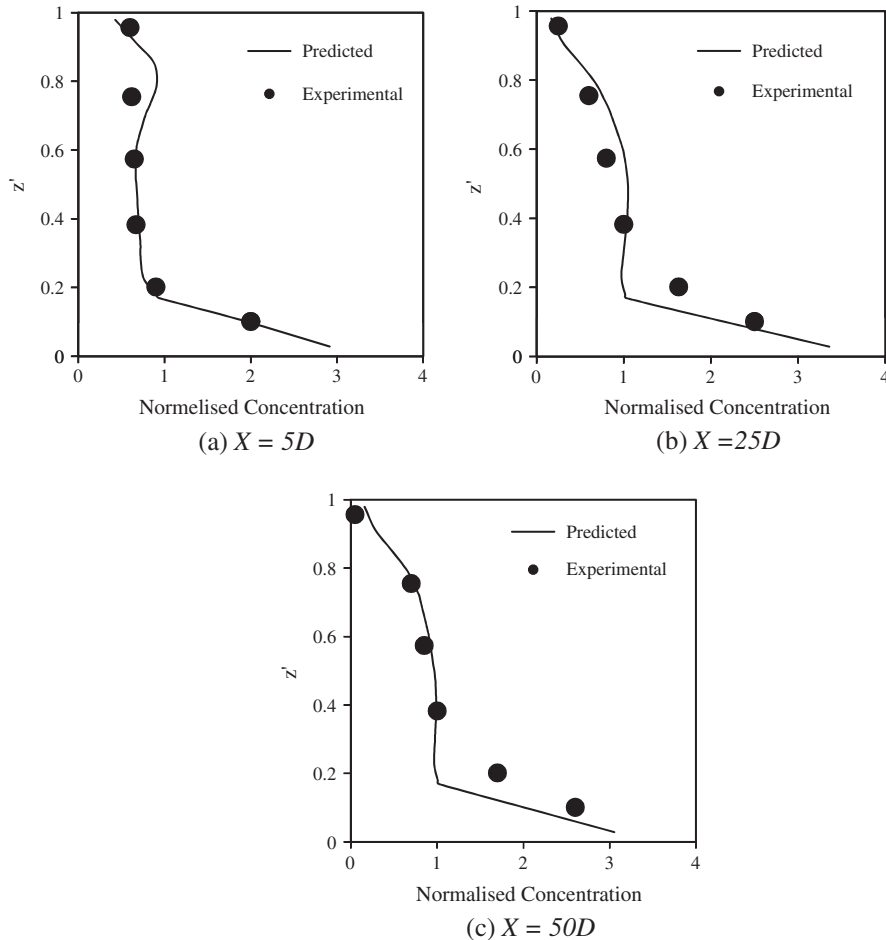


Fig. 25. Comparison between measured and predicted mid-vertical concentration profiles at different locations in the downstream of bend exit at $C_{vf} = 3.94\%$ and $V_m = 3.56 \text{ m/s}$ (Normalized concentration = $\alpha_s(z')/C_{vf}$).

Parametric analysis was undertaken to assess the sensitivity of simulation results to various input parameters and to determine appropriate default parameters and methodologies for predicting the different properties of slurry flow through pipeline.

5. Modeling results

5.1. Pressure drop for single-phase flow at different radius ratios

The pressure drops are presented in the normalized form [= $\Delta p / (\rho_w V_m^2 / 2)$], where, Δp is the pressure drop with reference to 32D upstream of bend inlet, ρ_w is the density of water and V_m is the mean flow velocity calculated by dividing the measured discharge by pipe cross-sectional area. Normalized pressure drops have been evaluated for simulated geometry for seven pipe bends at five mean flow velocities from 0.89, 1.34, 1.78, 2.67, up to 3.56 m/s. The corresponding range of Reynolds number is $(0.64 \times 10^5 - 2.50 \times 10^5)$. Pressure drop distributions obtained by experiments and CFD modeling for flow of water are presented in Fig. 4 for $R/r = 5.60$ at the flow velocity of 3.56 m/s. As expected, the pressure decreases along the flow constantly before the bend. However, as the flow reaches near the bend, the pressure decreases rapidly in comparison to the straight section. Figs. 5 and 6 show the pressure changes across the horizontal bend cross-section. The increased pressure at the outer wall of the bend is due to vortex formation.

The total bend loss coefficient (k_t) is defined as

$$k_t = \frac{\Delta p_t}{\left(\frac{\rho_w V_m^2}{2}\right)} \quad (48)$$

where Δp_t is the bend pressure drop.

The measured and simulated bend loss coefficients (k_t) are evaluated for each run and drawn graphically in Fig. 7. It is also observed that values of k_t reduce from a highest value for the elbow having radius ratio 0.0 to the lowest value for the radius ratio 5.60 and increase thereafter, a feature observed at all flow rates. The high pressure loss in a sharp elbow can be attributed to the generation of strong secondary flows due to the sharp turn. It is observed that the CFD modeling gives fairly accurate predictions (with percentage error in the range of $\pm 10\%$) for k_t at all flow velocities considered in the present study. In the present case, $R/D > 1.2 \times 10^4 < R_e < 4 \times 10^5$, Ito (1960) gave following correlation for k_t :

$$k_t = \frac{0.3897 \{0.95 + 4.42/(R/D)^{1.96}\} (R/D)^{0.84}}{R_e^{0.17}}, \quad R_e/(R/D)^2 > 364 \quad (49)$$

where $R_e = \frac{V_m D}{\nu}$, ν is kinematic viscosity of water.

It is observed that both the measured and CFD predictions for rough bends used in the present experiment are larger than the values predicted by Ito (1960) for smooth bends as shown in Fig. 8. Such a difference is obvious due to roughness of pipe bends.

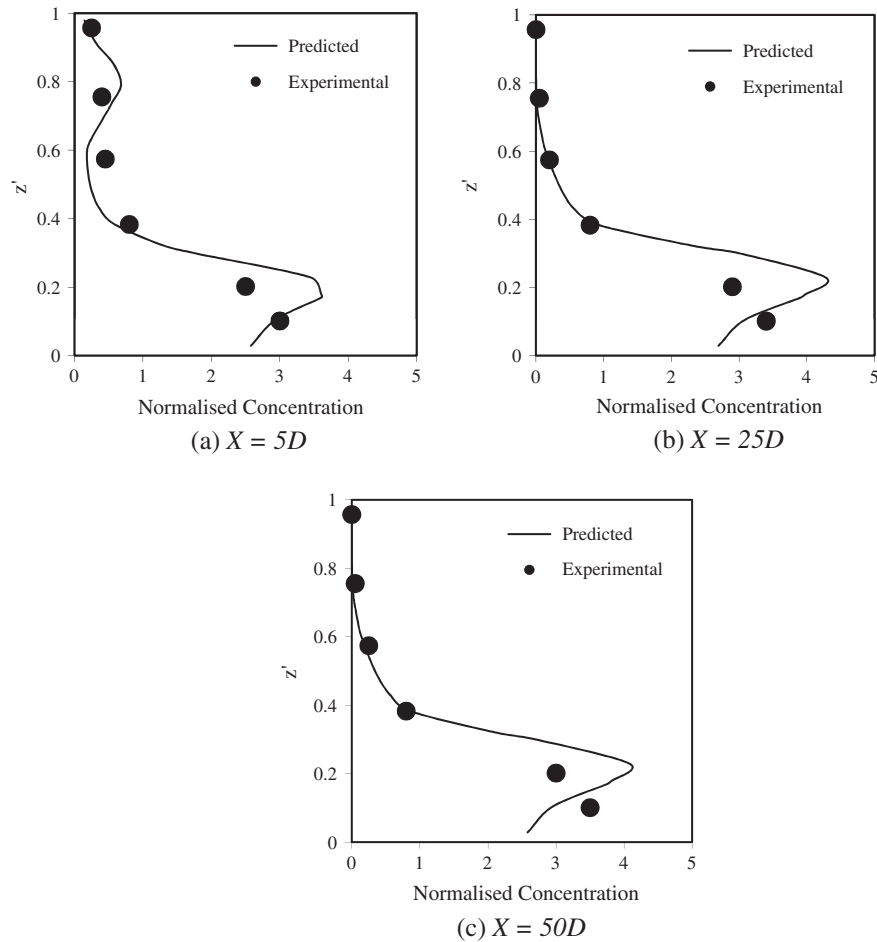


Fig. 26. Comparison between measured and predicted mid-vertical concentration profiles at different locations in the downstream of bend exit at $C_{vf} = 8.82\%$ and $V_m = 1.78 \text{ m/s}$ (Normalized concentration = $\alpha_s(z')/C_{vf}$).

However, CFD predictions are well in line with Ito (1960) correlation for smooth bends and experimental data for rough bends as shown in Fig. 8.

5.2. Pressure drop for slurry flow in bend having R/r of 5.60

The pressure drops in mid-horizontal plane are presented in Fig. 9 in the normalized form as $\Delta p/(\rho_m V_m^2/2)$, where Δp is the pressure drop with reference to the 32D upstream of bend inlet at a particular point, ρ_m is the measured density of slurry, V_m is the mean flow velocity calculated by dividing the measured discharge by pipe cross-sectional area for efflux concentration of 3.94–16.28% at flow velocities of 1.78 and 3.56 m/s.

Comparison between measured and predicted normalized pressure drops is shown in Figs. 10–12. From these figures, it is clearly seen that the CFD can predict the pressure drop with fair accuracy for slurry flow through horizontal 90 degree bend. However, as the efflux concentration increases, the CFD results begin to deviate from the measured values. The deviation increases with the concentration. It is observed that the CFD modeling gives predictions with percentage error in the range of $\pm 10\%$ for pressure drop at all flow velocities considered in the present study.

The measured and predicted bend loss coefficients (k_t) are drawn graphically in Fig. 13. It is observed that k_t reduces with increase in flow velocity, and decrease in efflux concentration. It is observed that the CFD modeling gives fairly accurate predictions (with percentage error in the range of $\pm 10\%$ except few data at

higher concentration) for k_t at all flow velocities considered in the present study.

5.3. Concentration distribution at bend

Cross-sectional concentration distributions (α_s) as predicted by CFD at six different locations (namely, bend inlet, bend centre, bend exit, $X = 5D$, $25D$ and $50D$, where X is the distance from bend exit) for efflux concentration 3.94%, 8.82% and 16.28% at flow velocities 1.78 m/s, 2.67 m/s and 3.56 m/s are shown in Figs. 14–16. In these figures, left hand side represents the outer wall, whereas right hand side represents inner wall of the bend. The concentration distributions are skewed towards the bottom and this skewness being higher for lower velocity of 1.78 m/s. At higher velocities of 2.67 m/s and 3.56 m/s, the concentration distribution is more uniform. At bend centre, bend exit and $X = 5D$, the particles are forced outwards due to the secondary flow. This secondary flow influences the motion of particles even after the bend and the increased concentrations at the outer wall of bend can be clearly seen at these locations for all the concentrations and flow velocities (Figs. 14–16). This effect is maximum at $X = 5D$ resulting into a central zone of very low concentration at the centre of pipeline. It is observed that in upstream side of bend inlet, $X = 25D$ and $X = 50D$, flow behavior is almost similar to the flow in straight section. The concentration profile becomes more uniform downstream of bend exit. This effect is more visible with increasing flow velocity as the increased strength of turbulent eddies

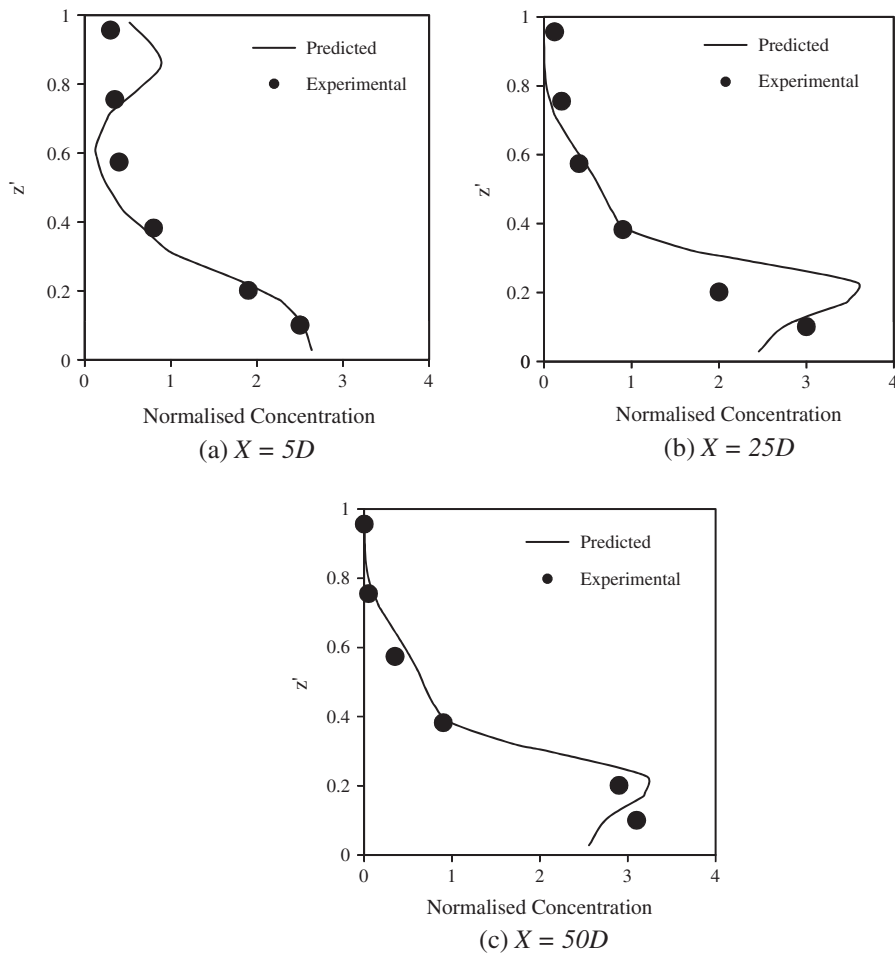


Fig. 27. Comparison between measured and predicted mid-vertical concentration profiles at different locations in the downstream of bend exit at $C_{vf} = 8.82\%$ and $V_m = 2.67 \text{ m/s}$ (Normalized concentration = $\alpha_s(z')/C_{vf}$).

formed due to the change in flow direction. However, at the bend inlet, the concentration profile does not deviate much from that in the upstream side.

In Fig. 17, distributions of v_{fz} and v_{sz} in m/s at $C_{vf} = 8.82\%$ and $V_m = 3.56 \text{ m/s}$ are shown. Deformation in velocity profiles due to the presence of bend is more prominent at bend centre, bend exit and $X = 5D$. Zone of higher velocity is shifted away from centre at these locations. Such deformation in velocity profile may be attributed to the secondary flow. However, at bend inlet, bend exit and $X = 5D$, zone of higher velocity remains in the central core of pipe cross-section.

Figs. 18–20 show the contours of magnitude and directions of velocity component in the plane perpendicular to the flow direction in m/s for $C_{vf} = 8.82\%$ and $V_m = 3.56 \text{ m/s}$ at bend centre, bend exit and $X = 5D$, respectively. Secondary flow begins to develop at bend centre (Fig. 18), it is fully developed at bend exit (Fig. 19) and remains developed at $X = 5D$ (Fig. 20). However, the velocity components in the plane perpendicular to the flow direction at bend inlet, $X = 25D$ and $X = 50D$ are negligible ($0\text{--}0.1 \text{ m/s}$ for $V_m = 3.56 \text{ m/s}$) due to the absence of secondary flows at these locations.

The observations made previously from Figs. 14–20 are reaffirmed in Fig. 21 showing the z -component of velocity for water and sand. High values at bend centre, bend exit and $X = 5D$ reflects strong effect of secondary flows. This effect creates zones of positive and negative values at left (outer wall of bend) and right (inner wall of bend) corner in the upper half of pipeline, respectively.

Positive zone situated at outer wall of bend is more prominent at bend centre due to free passage for water and sand particles (Figs. 21a and d and 16b). The diminishing of positive zone at $X = 5D$ may be attributed to the movement of sand particles into the positive zone situated at the outer wall of bend hindering the movement of more water and sand particles due to gravitational effects (Figs. 21c and f and 16b). Negative zone situated at the inner wall of bend is more prominent at $X = 5D$ as the gravitational effect and the presence of sand particles enhances the downward movement of water and sand particles (Figs. 21c and f and 16b). Negative zone situated at inner wall at bend centre is not prominent due to absence of sand particles (Figs. 21a and d and 16b). Very low values of $v_{fz}(x, y)$ and $v_{sz}(x, y)$ at bend inlet, $X = 25D$ and $X = 50D$ reflect diminishing effect due to the secondary flows are not shown in this figure.

Fig. 22 shows the contours of z component of slip velocity (difference in z components of velocity for sand and water) in the plane perpendicular to the direction of flow in m/s for $C_{vf} = 8.82\%$ and $V_m = 3.56 \text{ m/s}$. At bend centre, velocity component of sand is more than that of water, forcing sand particles towards outer wall of bend (Fig. 16b). These particles are trapped in secondary flows and move further up along the pipe wall. The positive slip velocity in the outer periphery as shown in Fig. 22b and c at bend exit and $X = 5D$ keeps more particles moving in the outer ring near pipe wall.

Particles segregate in a small portion of the pipe cross-section close to the outer wall in bend due to the action of centrifugal forces. These particles impinging on the outer wall, form a

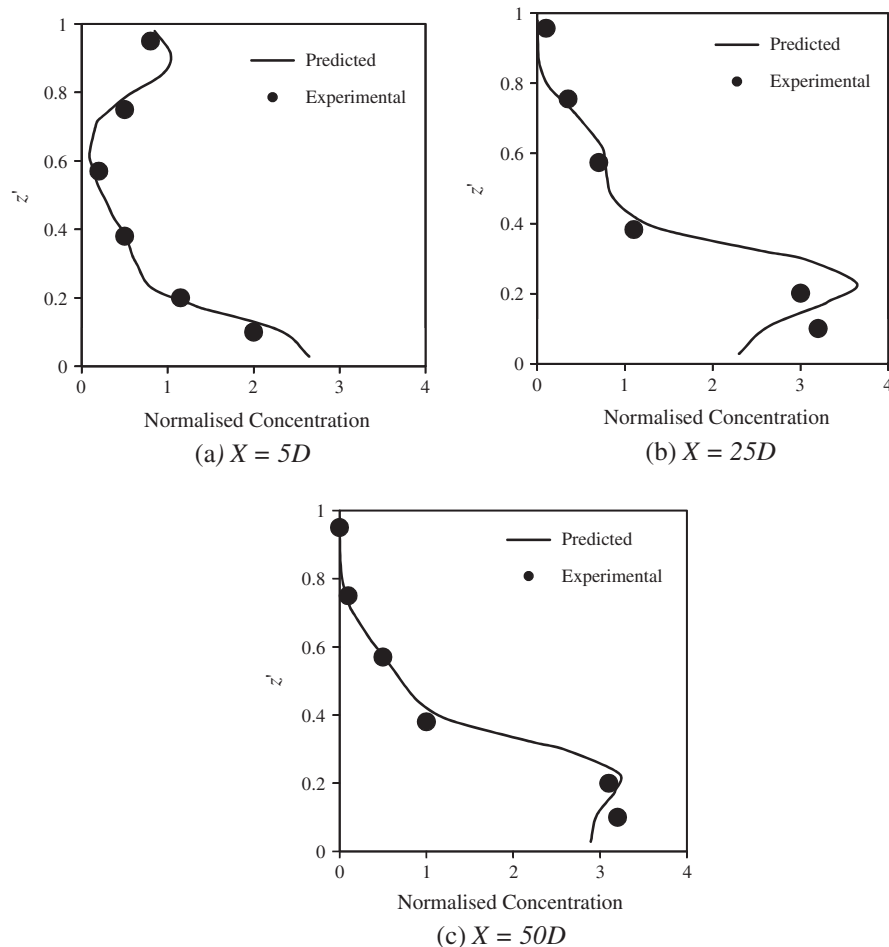


Fig. 28. Comparison between measured and predicted mid-vertical concentration profiles at different locations in the downstream of bend exit at $C_{vf} = 8.82\%$ and $V_m = 3.56 \text{ m/s}$ (Normalized concentration = $\alpha_s(z')/C_{vf}$).

relatively dense phase structure in a small portion of the pipe cross-section close to the outer wall that is termed as rope (concentration distributions at bend centre and bend exit shown in Figs. 14–16). Just after the bend, transport of particles is mainly due to the roping effect. The region of the rope has a much higher solid concentration than the remainder of the pipe. This high concentration increases the particle–particle collisions and causes the particles to decelerate. In other words, increased solids pressure results into the decrease in momentum of the particles (velocity distributions at bend centre, bend exit and $X = 5D$ shown in Figs. 18–21). The ropes were dispersed further down the bend where the particles accelerate and a secondary flow carries them around the pipe circumference and eventually to the middle of the pipe where turbulence causes them to spread over the entire cross-section (concentration distributions at $X = 5D$ in Figs. 14–16).

An overall review based on the above discussion for the concentration distribution of mono-dispersed slurry at different locations in the bend having radius ratio 5.60 reveals the following:

- The re-distribution of solid particles takes place downstream of the bend due to the secondary flows. This effect is seen close to the bend and decays with increase in distance.
- The concentration distribution is more uniform just downstream of the bend. The skewness in the concentration profile increases with downstream distance from the bend exit.

c. At the bend inlet, the concentration profile does not deviate much from that in the upstream side.

In the present study, α_s is measured at $X = 5D$, $25D$ and $50D$ from bend exit using sampling tubes C1, C2 and C3 (Fig. 2) at $z' = 0.094, 0.189, 0.377, 0.566, 0.755$ and 0.943 . Figs. 23–28 present the measured and predicted normalized solids concentration profiles using CFD in mid-vertical plane in downstream side of bend for flow velocities of $1.78, 2.67$ and 3.56 m/s at solid concentrations of 3.94% and 8.82% . In the present study, the concentration profiles measured at the same plane are used for comparison. The swirling flow due to secondary flow at bend makes the concentration at the top of pipe higher than that in central core near the bend exit at $X = 5D$. Figs. 23–28 exhibit reasonably good agreement between experimental and modeling values except for few cases.

6. Conclusions

The ability of implemented Eulerian model in FLUENT software to predict the pressure drop and concentration profile across a 90° horizontal pipe bend in slurry pipeline transporting silica sand using standard input parameters was investigated. Overall, there was broad qualitative and quantitative agreement in trends and flow patterns. The results suggest that the Eulerian model is rea-

sonably effective with the slurry pipe bend in the horizontal plane. We examine the possibility of FLUENT software when it is applied to slurry flow in a bend. In this software, $k-\varepsilon$ model is used to obtain fluid Reynolds stresses and the kinetic theory model is used to obtain solid phase stresses like fluid molecular stresses. These equations are solved coupling with other equations. We could get many interesting results by this approach, which are comparable to the measurements.

Followings are the specific conclusions based on the present study:

- i. Measured and predicted normalized pressure drop and bend loss coefficient show good agreement for flow of water in a wide range of R/r values from 0 to 5.89, with a maximum $\pm 10\%$ difference.
- ii. CFD modeling gives fairly accurate pressure drops (within percentage error of $\pm 10\%$ except few data at higher concentration) for the flow of silica sand slurry having particle diameter of 450 μm in the efflux concentration from 0% to 16.28% at different flow velocities from 1.78 to 3.56 m/s.
- iii. Velocity and concentration distributions of solids get almost uniform shortly after the bend.
- iv. The redistribution of solid particles takes place downstream of the bend due to the secondary flows. This effect is seen close to the bend exit, and with increase in distance this effect decays in the mid-vertical plane.

References

- Benyahia, S., Syamlal, M., O'Brien, T.J., 2007. Study of the ability of multiphase continuum models to predict core-annulus flow. *AIChE J.* 53, 2549–2568.
- Cebeci, T., Bradshaw, P., 1977. Momentum Transfer in Boundary Layers. Hemisphere Publishing Corporation, New York.
- Ding, J., Gidaspow, D., 1990. A bubbling fluidization model using kinetic theory of granular flow. *AIChE J.* 36, 523–538.
- Drew, D.A., Lahey, R.T., 1993. Particulate Two – Phase Flow. Butterworth-Heinemann Publications, Boston, pp. 509–566.
- FLUENT, 2006. User's Guide Fluent 6.2. Fluent Incorporation, USA.
- Garside, J., Al-Dibouni, M.R., 1977. Velocity-voidage relationships for fluidization and sedimentation. *I & EC Process Des. Dev.* 16, 206–214.
- Gidaspow, D., Bezburuah, R., Ding, J., 1992. Hydrodynamics of circulating fluidized beds, kinetic theory approach in fluidization VII. In: Proceedings of the 7th Engineering Foundation Conference on Fluidization.
- Ito, H., 1960. Pressure losses in smooth pipe bends. *J. Basic Eng. ASME* 82D, 131–143.
- Johnson, P., Jackson, R., 1987. Frictional-collisional constitutive relations for granular materials, with application to plane shearing. *J. Fluid Mech.* 176, 67–93.
- Kalyanraman, K., Ghosh, D.P., Rao, A.J., 1973. Characteristics of sand water slurry in 90° horizontal pipe bend. *Inst. Eng. (India) J.* 54, 73–79.
- Kaushal, D.R., Tomita, Y., 2002. Solids concentration profiles and pressure drop in pipeline flow of multisized particulate slurries. *Int. J. Multiphase Flow* 28, 1697–1717.
- Kumar, A., 2010. Experimental and CFD Modeling of Hydraulic and Pneumatic Conveying through Pipeline. Ph.D. Thesis. I.I.T. Delhi.
- Kumar, A., Kaushal, D.R., Kumar, U., 2008. Bend pressure drop experiments compared with FLUENT. *Inst. Civil Eng. J. Eng. Comput. Mech.* 161, 35–45.
- Launder, B.E., Spalding, D.B., 1974. The numerical computation of turbulent flows. *Comput. Meth. Appl. Mech. Eng.* 3, 269–289.
- Ling, J., Skudarnov, P.V., Lin, C.X., Ebadian, M.A., 2003. Numerical investigations of liquid-solid slurry flows in a fully developed turbulent flow region. *Int. J. Heat Fluid Flow* 24, 389–398.
- Lun, C.K.K., Savage, S.B., Jeffrey, D.J., Chepurniy, N., 1984. Kinetic theories for granular flow: inelastic particles in couette flow and slightly inelastic particles in a general flow field. *J. Fluid Mech.* 140, 223–256.
- Pain, C.C., Mansoorzadeh, S., de Oliveira, C.R.E., 2001. A study of bubbling and slugging fluidised beds using the two-fluid granular temperature model. *Int. J. Multiphase Flow* 27, 527–551.
- Richardson, J.R., Zaki, W.N., 1954. Sedimentation and fluidization: Part I. *Trans. Inst. Chem. Eng.* 32, 35–53.
- Schaan, J., Sumner, R.J., Gillies, R.G., Shook, C.A., 2000. The effect of particle shape on pipeline friction for Newtonian slurries of fine particles. *Can. J. Chem. Eng.* 78, 717–725.
- Schaeffer, D.G., 1987. Instability in the evolution equations describing incompressible granular flow. *J. Diff. Eq.* 66, 19–50.
- Syamlal, M., Rogers, W., O'Brien, T.J., 1993. MFIX Documentation. Theory Guide, vol. 1. National Technical Information Service, Springfield, VA.
- Thinglas, T., Kaushal, D.R., 2008a. Comparison of two dimensional and three dimensional CFD modeling of invert trap configuration to be used in sewer solid management. *Particuology* 6, 176–184.
- Thinglas, T., Kaushal, D.R., 2008b. Three dimensional CFD modeling for optimization of invert trap configuration to be used in sewer solid management. *Particulate Sci. Technol.* 26, 507–519.
- Toda, M., Kamori, N., Saito, S., Maeda, S., 1972. Hydraulic conveying of solids through pipe bends. *J. Chem. Eng. Jpn.* 5, 4–13.
- Turian, R.M., Ma, T.W., Hsu, F.L., Sung, D.J., Plackmann, G.W., 1998. Flow of concentrated non-Newtonian slurries: 2. Friction losses for flow in bends, fittings, valves and Venturi meters. *Int. J. Multiphase Flow* 24, 243–269.